Evaluation of Mie scatter approximation formulas for the scattering of infrared light at biological cells

Ketil Breckan Thovsen

Norwegian University of Life Sciences
Department of Mathematical Sciences and Technology
Master Thesis 30 credits 2013

Evaluation of Mie scatter approximation formulas for the scattering of infrared light at biological cells

Norwegian University of Life Sciences
Dept. of Mathematical Sciences and Technology

Ketil B. Thovsen

Supervisor: Achim Kohler

May 14, 2013

Abstract

Infrared (IR) spectroscopy has during recent years become a very attractive method for biochemical analysis of cells and tissue, since it can be applied in biological material without destroying its native structure. Since the wavelength of infrared light is comparable to the radius of cells and cell compounds, absorbance spectra are hampered with strong scattering effects, making biochemical interpretation and subsequent data analysis difficult. Since scattering at cells and cell compounds can be approximated by formulas for the scattering of spherical particles, the scatter effects can be approximated by Mie scattering. The exact Mie formula demand extensive computation and make physical interpretations of the scattering effects difficult. In the literature several Mie scattering approximation formulas have been discussed. These approximation formulas have different validity ranges for parameters such as wavelength region and scattering angles. The aim of this thesis was to evaluate different approximation formulas for scattering of infrared light at cells and to interpret the basis for these approximation formulas for situations where not only forward scattering is considered. This is highly relevant for FTIR microscopes which have a high numerical aperture.

It is shown that scattering with $\theta < \theta_{\mathrm{NA}}$ can be well estimated using the Penndorf, Shifrin and Punina approximation for scattered light at angles $\theta \in [1^o, 10^o]$ and the Gordon approximation for scattered light at angles $\theta \in [11^o, \theta_{\mathrm{NA}}]$. An approach which interpolate both approximations is therefore suggested.

Different types of oscillations in the scatter extinction have been investigated and explained in terms of ray dynamics. The exact Mie solution contain resonances as ripples which the approximation formulas do not exhibit. The resonances giving the ripples are explained by ray dynamics where the respective rays enter and leave the sphere in the same direction. Signatures of rays obtained by refraction, can be visualized in the Fourier transform of the extinction curve. For example a triangular ray is expected to appear for refractive indices above $m = 2.0$ and is determined in the Fourier transform of the extinction. A semiclassical approach, following the rules of quantum mechanics, is used to explain rays that correspond to bound states in the corresponding quantum mechanical case.

Sammendrag

Infrarød spektroskopi har gjennom de siste årene blitt en populær metode for biokjemisk analyse av celler og vev, siden det kan bli brukt på biologisk materiale uten å ødelegge dets opprinnelige struktur. Siden bølgelengden på infrarødt lys er i størrelsesorden radius på en celle og dens organeller, vil absorbansspektra bli ødelagt av et sterkt bidrag fra lysspredning, noe som gjør biokjemisk analyse vanskelig. Siden lysspredning i celler og dens organeller kan bli estimert av formler for lysspredning av sfæriske partikler, kan lysspredningsbidraget bli estimert som Mie spredning. De eksakte Mie løsningene krever stor beregningskapasitet, og gjør tolkning av lysspredningsbidraget vankelig. Mange approksimasjonsformler for Mie spredning har blitt foreslått. Disse har forskjellig gyldighetsområde for parametre som bølgelengdeområde og spredningsvinkel. Formålet med denne oppgaven er å studere forskjellige approksimasjonsformler for spredning av infrarødt lys i celler og evaluere grunnlaget for å bruke disse ved forskjellige spredningsvinkler. Dette har betydning for FTIR mikroskopi med objektiver som dekker en stor romvinkel.

Oppgaven viser at spredning ved $\theta < \theta_{\mathrm{NA}}$ kan estimeres ved å bruke Penndorf, Shifrin of Puninas approksimasjonsformel for spredt lys med vinkel $\theta \in [1^o, 10^o]$ og Gordons approximasjonsformel for spredt lys med vinkel $\theta \in [11^o, \theta_{\mathrm{NA}}]$. En metode som interpolerer disse metodene er derfor foreslått.

Forskjellige typer oscillasjoner i ekstinksjonskurven har blitt undersøkt od forklart ved hjelp av stråledynamikk. Den eksakte Mie løsningen inneholder resonanser i form av skarpe tagger, som approksimasjonsformlene ikke viser. Resonansene som gir taggene blir forklart ved hjelp av stråledynamikk, der strålene går inn i og ut av den sfæriske partikkelen i samme retning. Ved å Fourier transformere ekstinksjonskurven, kan signaturene fra resonansene som kan oppnås ved hjelp av brytning, visualiseres. For eksempel kan en triangulær stråle sees ved brytningsindeks $m = 2.0$. Denne er funnet i Fourier transformen av ekstinksjonskurven. En semiklassisk fremgangsmåte, som følger lovene til kvantemekanikken, brukes til å forklare stråler som bundene tilstander i det kvantemekaniske tilstanden.

Preface

This thesis has been written during the three and a half months of the spring semester 2013, and the submission of the thesis marks the end of my master's degree of environmental physics and renewable energy at the Norwegian University of Life Sciences.

When first deciding on the topic for my master thesis the spring of 2012, I knew little about infrared spectroscopy and light scattering by cells. The year that has past since then, has been a challenging and very interesting learning process that has culminated in this thesis. It has also given me an interest in infrared spectroscopy and light scattering, and related fields. The topics of the thesis touches into many fields of physics, such as electromagnetic theory, optics, classical mechanics and quantum mechanics. The use of these different fields has tested and evolved my knowledge of theory learned in several physics courses during my years as a student.

For being able to complete my work, there are several people to thank:

First of all i would like to give a great thanks to my supervisor Achim Kohler for valuable help in completing my thesis, and taking the time to answer all my questions, even when stopping by his office unannounced. Also the members of his research team, including Reinhold Blümel at the Wesleyan University, deserves thanks for helpful input and advice.

Secondly my family and friends deserves a thanks for valuable moral support. And last but not least I would like to thank my girlfriend Mari for being helpful and understanding when the work on my thesis has consumed much of my time, leaving other tasks neglected.

Ketil B. Thovsen

Oslo, May 13th, 2013

Contents

1 Introduction

1.1 Motivation

Infrared spectroscopy is an established method for chemical and biochemical analysis of samples with a wide range of applications, e.g. in organic and inorganic chemistry, forensic science, biology, biomedicine and material science [1–5]. By probing the sample with infrared light, an absorption spectrum is achieved, which contains information about the functional groups in the sample. By interpretation of spectral bands of functional groups, compounds or single functional groups can be identified [6]. In biology and biomedical sciences pattern recognition methods are used to separate e.g. diseased cells from healthy cells on the basis of structural changes in biomolecules or differences in composition of compounds in cells. [2, 5, 7].

Chemical absorption bands in infrared spectroscopy of cells are often interfered by light scattering. Cells, cell compounds such as cell nuclei and organelles, which have similar size as the wavelength of the infrared light ($\sim 10\mu m$), are highly scattering particles [5]. The size of the cell also causes problems with regard to probing the cell with a high enough flux of light to achieve an acceptable signal-to-noise ratio (statistical fluctuations in the spectrum reaching the sensor). This problem is solved by using a synchrotron light source (sec. 2.5.2) and a microscope (sec. 2.5.1) to focus the light near the diffraction limit (about $2\lambda/3 - \lambda/2$) [7]. The commonly used term for this type of spectroscopy is infrared microspectroscopy, which is described is section 2.5.

The light scattering in infrared spectra of single cells has been interpreted as Mie scattering, since the distortions in the spectra resemble the scattering curve predicted by the Mie scattering theory, which describes scattering of electromagnetic light at spheres [5]. Using the Mie scattering theory to estimate the scattering by biological particles proposes practical problems. The Mie scattering formulas depend on the refractive index and size of the particles, which in most cases are unknown. Also, the Mie formulas are complicated, and require extensive computation, which makes an it-

erative comparisons of the Mie scattering with the distortion in the spectra unfeasible. Approximations to the Mie scattering formulas are therefore valuable. Approximation formulas may speed up numerical algorithms for correcting Mie-type scattering contributions. In addition they may provide insight in the physical interpretation of scattering, which is often difficult to obtain from the exact Mie theory.

Several approaches for using approximation formulas to estimate the Mie scattering contribution to the absorption spectra has been made [1, 2, 8–10]. An example is an approach for estimating the Mie scattering contribution, called Extended Multiplicative Signal correction (EMSC), was proposed by Kohler et al. [10]. This approach uses multivariate methods to find the most suitable of many approximated Mie scattering curves, without knowing the radius and refractive index. Later this approach was extended to also take into consideration the strong relationship between the absorption and the refractive index, which is basically two of the same [1] (sec. 2.2). A more thorough introduction to the EMSC approach is found in the references [1, 2, 8–10].

Most of the EMSC approaches uses an approximation formula stated by van de Hulst [11] (eq. 3.10) to estimate the Mie scattering contribution to the transmitted spectrum. This formula is an estimation of the extinction in the forward direction. In the case where no scattering occur, the extinction equals the absorbed light. In the case where some of the light is scattered away from the incident direction, the extinction equals the scattered light plus the absorbed light (sec. 2.3.1).

The approximation formula also works under the assumption that all the transmitted light reaching the sensor is propagating in the same direction as the incident light (sec. 3.2.1). For infrared microspectroscopy, this is not the case. The focusing optics of the microscope collects a significant amount of the scattered light, meaning that the approximation formula used in the EMSC approach will overestimate the scattering contribution to the absorption spectra, made by the spherical particles. Approximation methods for estimating the scattering in a non-forward direction will therefore also be of interest.

The goal of this thesis is to evaluate the scattering from spheres in the forward and non-forward direction, and attempt to estimate the scattering which falls in the area of the focusing optics during microspectrocopic analysis of cells. This is done using approximations and comparing them to the exact Mie solution. An important issue in this evaluation is to discuss the validity of the approximation and the physical assumptions they are based on. Secondly this thesis will discuss the sharp resonance structures, referred to as ripples, which can be seen in the exact Mie solution, but which are not explained by the approximations presented.

1.2 Outline

This thesis is divided into 5 chapters making representing the main topics of the thesis. Chapter 2 will thoroughly present the general theory of light scattering, absorption of infrared light in dielectric material and the general working principle of microspectroscopy with a synchrotron light source. Also the Mie solution to light scattering by spheres of arbitrary size is presented. Chapter 2 will give the physical principles and technology on which this thesis is based. In addition it provides a presentation of the relationship between light scattering and absorption, which is given by a refractive index containing a real and an imaginary part, describing the refractive and absorptive properties of the material.

Chapter 3 presents an algorithm for numerical computation of the exact Mie solutions. Further it presents a variety of approximations to the real solution:

1. The anomalous diffraction approximation (sec. 3.2.1) which is the approximation proposed by van de Hulst [11], valid for values of the refractive index of the scatterer near the refractive index of the ambient medium.

2. An approximation by Wiscombe [12] (sec. 3.2.2), applied in the forward direction, valid for low values of the size parameter ($x = ka \to 0$), where the size parameter is defined as the product of the radius a of the sphere and the wavenumber k of the incident light.

3. An approximation by Blümel [13], also applied in the forward direction, and with the same region of validity as Wiscombe's approximation. Blümel's and Wiscombe's approximations are compared in sec. 3.2.2.

4. The Penndorf-Shifrin-Punina (PSP) approximation [14] (sec. 3.3.1) which approximates Mie scattering in a non-forward direction, but preferably at low scattering angles.

5. The Fymat-Mease (FM) approximation [14] (sec. 3.3.1) , which is an extension of the PSP approximation. This also in a non-forward direction, but at low scattering angles.

6. An approximation by Gordon [15] (sec. 3.3.2), which approximates Mie scattering in the non-forward direction, at larger angles than the PSP and FM approximation.

In section 3.4 approximations 4, 5 and 6 are integrated over a range of solid angles and compared to the exact solution. In section 3.12 the anomalous diffraction approximation is applied within the frames of the PSP and Gordon approximation, as an attempt to apply the forward version of the anomalous diffraction in the non

forward direction. In section 3.13 an example of application is given.

Chapter 4 presents the theoretical origin of the sharp ripples on the underlying curve seen in the exact solution. The ripples are discussed in light of the ray image of the classical theory, also including a semiclassical approach corresponding to the quantum mechanical scattering problem. Where the ripples are present in the approximations from chapter 3, they are compared to the exact solution.

2 Theoretical background

2.1 Introductory remarks

- In infrared spectroscopy, the convention for wavenumber notation is $\tilde{\nu}$, which is related to the wavelength λ by the equation [6]:

$$\tilde{\nu}[cm^{-1}] = \frac{10^4}{\lambda[\mu m]} \tag{2.1}$$

  The wavenumber $\tilde{\nu}$ denotes the number of wavelengths per centimeter.

- In general scattering theory the notation k is used for wavenumber, which is defined by van de Hulst [11] as:

$$k[cm^{-1}] = 2\pi\frac{10^4}{\lambda[\mu m]} \tag{2.2}$$

  The wavenumber k denotes the number of radians per centimeter. This last notation is the most used in this report, but the first one occurs when it is convenient.

- If not otherwise stated, the incident light can be assumed to be a plane unpolarized electromagnetic wave throughout this thesis. The mathematical description of the electric component of the wave is:

$$\mathbf{E}(\mathbf{r}, t) = E_0 \cos(\mathbf{k} \cdot \mathbf{r} - \omega t) = Re\{E_0 e^{i(\mathbf{k}\cdot\mathbf{r}-\omega t)}\} \tag{2.3}$$

  Where ω is the angular frequency, t is time, $\mathbf{k}$ is the vector wavenumber and E_0 is the amplitude of the electric field.

- If one views this wave from a fixed point $\mathbf{r}$ in space, e.g. a point charge in space, it is reasonable to define this fixed point as 0. The expression for the electromagnetic wave then is:

$$E(0, t) = Re\{E_0 e^{-i\omega t}\} \tag{2.4}$$

- If one on the other hand views the wave as an entire stationary wave, like in many scattering problems, we set $t = 0$, yielding the following expression for the electromagnetic wave:

$$E(\mathbf{k}, 0) = Re\{E_0 e^{i\mathbf{k}\cdot\mathbf{r}}\} \tag{2.5}$$

- The infrared (IR) region of the electromagnetic spectrum ranges from $\tilde{\nu} = 13\ 000\ cm^{-1}$ at the limit of visible light, to $\tilde{\nu} = 10\ cm^{-1}$ at the limit of the microwave region of the electromagnetic spectrum. The infrared region is divided into three subregions: Near-IR ($\tilde{\nu} = 13\ 000\ cm^{-1}$ to $4\ 000\ cm^{-1}$), mid-IR ($\tilde{\nu} = 4\ 000\ cm^{-1}$ to $200\ cm^{-1}$) and far-IR ($\tilde{\nu} = 200\ cm^{-1}$ to $10\ cm^{-1}$). The different regions can be applied in infrared spectroscopy, dependent on purpose [6]. This thesis emphasizes the mid-IR region, which is associated with the stretching and bending of functional groups.
- In the Mie scattering section (sec. 2.4) a dimensionless size parameter $x = ka$ is introduced. The variable x is the product of the wavenumber k (eq. 2.2) and the diameter a of the sphere. Other than the refractive index, the scattering is merely dependent on the variable x, and never the wavenumber or the radius alone. By this we can understand that the scattering of light by a sphere is scale invariant, meaning that the scattering of low frequency light by a large sphere is equivalent with the scattering high frequency light by a proportionally small sphere.

2.2 Absorption and dispersion

2.2.1 Absorption of infrared radiation[1]

A functional group in a molecule consisting of atoms engaging in valence bonds can be treated as a classical harmonic oscillator, where the valence bond represents a spring force holding the atom attached to its mother molecule. If there is a difference in net charge in the atoms in the functional group, this gives rise to a dipole moment, making it susceptible to the influence of an applied electrical field. An electromagnetic plane wave can be presented as an oscillating electrical field written as $\mathbf{E}(t) = Re\{E_0 e^{i\omega t}\}\hat{k}$ and magnetic field $\mathbf{B}(t) = Re\{B_0 e^{i\omega t}\}\hat{j}$, with $\hat{k}$ and $\hat{j}$ as the unit vectors in the z- and y-direction, and the wave propagating in the x-direction. The dipole (functional group) will experience a passing electromagnetic wave as a time-dependent force

[1] This classical representation of absorption of infrared light in a dielectric sample is mainly the same as the one presented in an article [16] and is based on the representation in the book on electrodynamics by David J. Griffiths [17]

given as $\mathbf{F} = q\left[\mathbf{E} + (\mathbf{v} \times \mathbf{B})\right]$, where $\mathbf{v}$ is the velocity vector of the particle relative to the magnetic field. Although since the magnetic flux amplitude $B_0 = E_0/c$ in an electromagnetic wave, where c is the speed of light, magnetic contribution to the Lorentz force is very small. Thus we can assume that the force acting upon the dipoles is purely electrical, and drop the vector notation: $F(t) = Re\{qE_o\ e^{-i\omega t}\}$.

The resonance frequency of the spring system is classically given in terms of the effective mass of the molecules in the spring system and the stiffness of the spring force holding the molecules together. The spring system can now be modeled as a driven oscillator including a damping force $m\gamma$. The damping is caused by transferring energy to other parts of the molecule and through dipole radiation. The model of the system is given by (Newtons 2. law):

$$q\ E_0 \cos(\omega t) = m\gamma \frac{dz(t)}{dt} + m\omega_0^2 z(t) + m\frac{d^2 z(t)}{dt^2} \tag{2.6}$$

Where $z(t)$ is the position of the molecule on the z-axis as a function of time, m is the mass, q is the charge of the molecule, E_0 is the amplitude of the electric field, γ is the damping constant, ω_0 is the resonance frequency and ω is the frequency of the electromagnetic wave. The inhomogeneous differential equation 2.6 has a particular solution which describes how the system responds to the force with time. If the damping is critical, the oscillation will go towards a steady state solution, which is the oscillation described by the time dependent offset from the equilibrium position z_0, and can be expressed as:

$$z(t) = z_0 \cos(\omega_0 t) = Re\{z_0 e^{i\omega_0 t}\} \tag{2.7}$$

Where ω_0 is the resonance frequency of the system and t the time.

The polarization p of the dipole is given as the offset from equilibrium times the difference in charge q, $p = qz(t)$. When the frequency of the electromagnetic wave ω is in the vicinity of the resonance frequency ω_0, the energy of the wave is absorbed as mechanical oscillations of the functional group. When light consisting of a continuous spectrum of frequencies is sent through a sample containing a specific functional group, the absorption of light will concentrate around the resonance frequency of the functional group, giving rise to an absorption band in the continuous spectrum.

The function $\tilde{z}$ is the offset from equilibrium $z(t)$ including both real and imaginary parts from equation 2.7 and $\tilde{E}$ is the electrical field $E(t)$ including both real and imaginary parts from equation 2.4. These complex functions are put into equation 2.6, and we obtain the complex dipole moment $\tilde{p} = q\tilde{z}$ as:

$$\tilde{p} = \frac{q^2/m}{\omega_0^2 - \omega^2 - i\gamma\omega}\tilde{E} \tag{2.8}$$

Where the m is the mass of the dipole particle, q is the charge, ω is the frequency of the incident light, γ is the damping constant and ω_0 is the resonance frequency of the spring system.

The polarization of a volume element with N dipoles and volume V is related to the complex electric susceptibility $\tilde{\chi}_e$ by:

$$\tilde{P} = \frac{N}{V}\tilde{p} = \varepsilon_0 \tilde{\chi}_e \tilde{E} \tag{2.9}$$

Where ε_0 is the dielectric constant of vacuum. The polarization of each molecule consisting of several dipoles is given by:

$$\tilde{p} = \sum_j \frac{q_j^2 f_j / m_j}{\omega_j^2 - \omega^2 - i\gamma\omega} \tilde{E} \tag{2.10}$$

Where j indicates type of dipole, f_j the number of this particular dipole in each molecule, m_j its mass, ω_j the resonance frequency of this type of dipole. The sum is over all types of dipoles in the molecule. The expression for the complex susceptibility can now be obtained by rearranging equation 2.9:

$$\tilde{\chi}_e = \frac{N\tilde{p}}{\varepsilon_0 \tilde{E}} = \frac{N}{\varepsilon_0} \sum_j \frac{q_j^2 f_j / m_j}{\omega_j^2 - \omega^2 - i\gamma\omega} \tag{2.11}$$

The relative dielectric constant ε_r is related to the susceptibility by $\varepsilon_r = 1 + \chi_e$. The relative dielectric constant for an absorbing medium is then given by:

$$\tilde{\varepsilon}_r = \bar{\varepsilon}_r + \frac{N}{\varepsilon_0} \sum_{j \epsilon IR} \frac{q_j^2 f_j / m_j}{\omega_j^2 - \omega^2 - i\gamma\omega} \tag{2.12}$$

Where $\bar{\varepsilon}_r$ is the real, non-dissipative part of the dielectric constant, while the sum in the second term stretches over the frequencies in the spectral region of infrared light. The absorption resonances above and below the infrared spectrum will not absorb light when the sample is illuminated by infrared light, but are included in the non-dissipative term expressed as:

$$\bar{\varepsilon}_r = 1 + \alpha(\omega) + \beta(\omega) \tag{2.13}$$

Where $\alpha(\omega)$ is the contribution to the dielectric constant by frequencies larger than the frequencies in the infrared area, and $\beta(\omega)$ is the contribution from those frequencies lower that those in the infrared area. This shows that absorption bands with resonance frequencies outside the spectral range of the light contribute to the real part of the refractive index m. The refractive index is given as:

$$m = \sqrt{\tilde{\varepsilon}_r} \tag{2.14}$$

A medium without absorption resonances at any freuency would have a refractive index $m = 1$, which would have made it an optical vacuum [18]. The presence of the absorption resonances is what makes the real part of the refractive index unequal to 1 and frequency dependent (dispersion).

A complex refractive index ($m = n + in'$) indicates absorption of radiative energy in the sample within the range of frequencies of the light the sample is exposed to. The real part of the complex refractive index n describes the refraction of light without energy loss, while the imaginary part describes dissipation of energy due to absorption of light.

2.2.2 Relationship between n and n'

In formula 2.13 we see that the part of the complex dielectric function $\tilde{\varepsilon}_r$ which contains the absorption bands outside the spectral range of the light in question, denoted $\bar{\varepsilon}_r$, also contributes to the dielectric function. This part of $\tilde{\varepsilon}_r$ is with no doubt real, and will only contribute to the real part of $\tilde{\varepsilon}_r$. The absorption resonances inside the spectral range has a real *and* an imaginary part, and will therefore also contributes to the real part of $\tilde{\varepsilon}_r$.

The real part ε, and imaginary part ε' of the complex dielectric constant $\tilde{\varepsilon}_r$ is related by the Kramers-Krönig relation. Since the complex refractive index $m = n + in'$ is related to the dielectric function by formula 2.14, this means that by knowing the absorption resonances in the medium one can obtain the non-linear refractive index. The Kramers-Krönig relation is given as [18]:

$$\varepsilon(\omega) = 1 + \frac{2}{\pi}\ \text{P.V.} \int_0^\infty \frac{\Omega\varepsilon'(\Omega)}{\Omega^2 - \omega^2} d\Omega \tag{2.15}$$

Where P.V. denotes Chauchy's principal value, which is the integral on the real axis from 0 to ∞ disregarding the singularity at $\Omega^2 = \omega^2$. The absorption resonance frequency is denoted by ω. The real part of the dielectric function for any solid or liquid is related to the imaginary part by 2.15. In figure 2.1 the dependence between n and n' is shown. The real part of the refractive index varies a lot in the vicinity of an absorption band, which can be seen in fig. 2.1 as an anti-symmetric curvature in the real part of m around the resonance frequency point, while the imaginary part shows a symmetric hump around the same point.

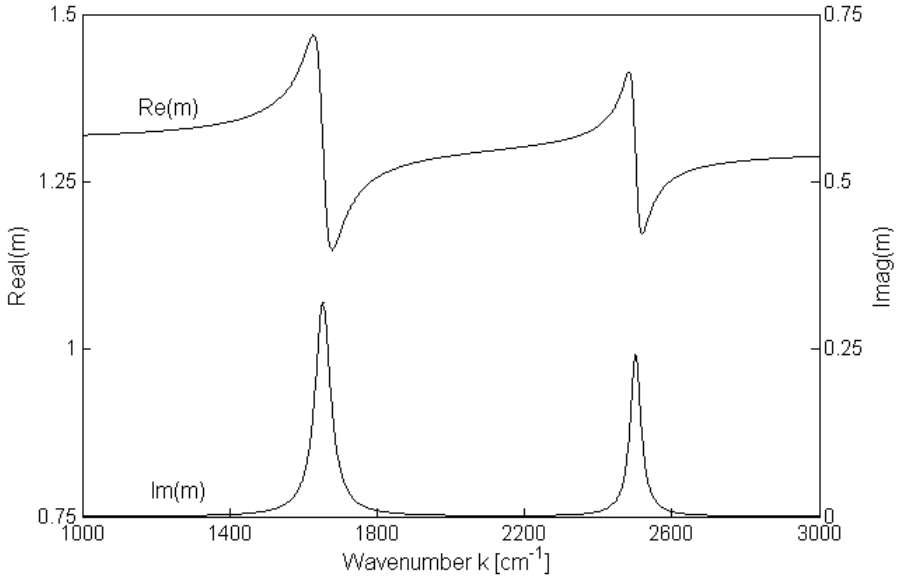

Figure 2.1: The curves shows the value of the real and imaginary part of the refractive index as a function of wavenumber k. The resonance frequencies is located at 1650 cm^{-1} and 2500cm^{-1}

2.3 Light scattering by spherical particles

2.3.1 Scattering and extinction formulas

If we assume an absorbing sphere illuminated exclusively by light from a distant source (no angular distribution in the incident light), then we can use the principle of conservation of energy to account for scattered and absorbed light. By scattered light we mean the light propagating at an angle relative to the incident light. The scattering angle θ, is the difference in angle between the line parallel to the incident light and the propagation of the scattered light. The angle φ describes the azimuth angle of the scattered light, shown in figure 2.2. In the case of an arbitrary shape of a particle, the scattering in any direction is described by four amplitude functions dependent on θ and φ, S_1, S_2, S_3 and S_4, that together form a scattering matrix $\mathbf{S}(\theta, \varphi)$. The electrical field components in the scattered electromagnetic wave parallel and perpendicular to the plane of scattering, are [11]:

$$\begin{pmatrix} E_{\parallel} \\ E_{\perp} \end{pmatrix} = \begin{pmatrix} S_2 & S_3 \\ S_4 & S_1 \end{pmatrix} \cdot \frac{e^{-ikr+ikz}}{ikr} \begin{pmatrix} E_{0\parallel} \\ E_{0\perp} \end{pmatrix} \tag{2.16}$$

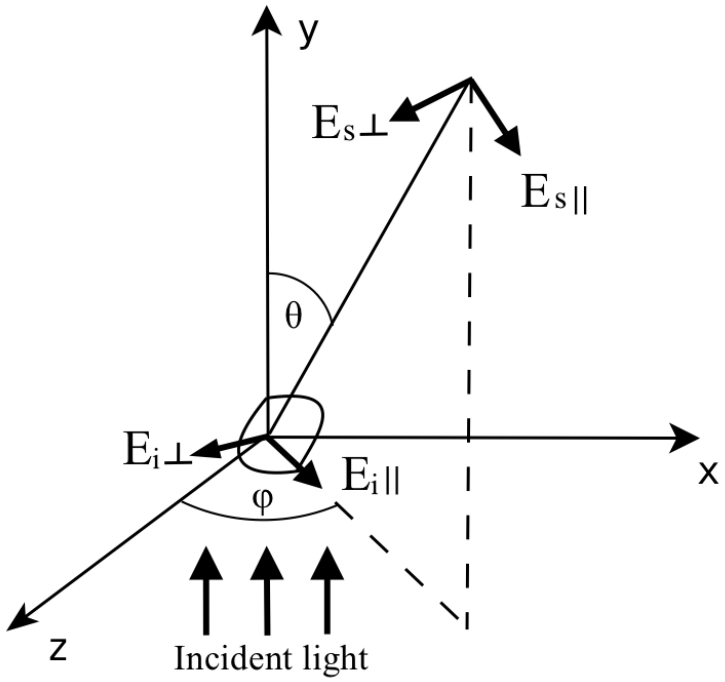

Figure 2.2: An arbitrarily shaped scatterer is hit by light propagating in the positive y-direction. The light has electric field components $E_{i\perp}$ perpendicular to the scattering plane and component $E_{i,\parallel}$ parallel to the scattering plane. The scattering plane is the plane defined by the y-axis and the azimuth angle φ. The scattered light has the electric field components $E_{s\perp}$ perpendicular to the scattering plane and $E_{s\parallel}$ parallel to the scattering plane. The angle θ is the scattering angle. Based on a figure in the book by Bohren and Huffman [18]

.

The elements $E_{\parallel}$ and $E_{\perp}$ corresponds to the parallel and perpendicular components of the electric field relative to the the plane of scattering.

The equation 2.16 is obtained by combining the expression for the incoming plane wave

$$E_i(z,t) = E_0 e^{-ikz+i\omega t}, \tag{2.17}$$

with the outgoing spherical wave

$$E_S(r,t) = E_0 \; S(\varphi,\theta)\frac{e^{-ikr+i\omega t}}{ikr} \tag{2.18}$$

for each direction of polarization. By replacing E_0 in eq. 2.18 with the expression for E_0 obtained from eq. 2.17, the time dependent terms vanishes, leaving the exponential term $e^{-ikr+ikz}/ikr$. The scattered field is now dependent on the incident field at z, but may be replaced by E_0 since $E_i(0) = E_0$. The incident and scattered wave is shown in figure 2.3.

The scattering cross section C_{sca} describes the area that needs to be covered up in the cross sectional area of the incident beam, to account for the light scattered away from the propagating direction of the incident beam. To obtain the scattering cross section, a dimensionless function $F(\theta, \varphi)$ has to be integrated over all directions [11]:

$$C_{sca} = \frac{1}{k^2} \int \int F(\theta, \varphi) \sin\theta \; d\theta \; d\varphi \tag{2.19}$$

Where k is the wavenumber. The function $F(\theta, \varphi)$ is later replaced by a function describing the intensity distribution, which is dependent on the amplitude functions $S(\theta, \varphi)$ describing the scattering components (phase and amplitude) of the scattered wave, relative to the scattering plane. The function $F(\theta, \varphi)$ is dependent on the shape of the particle, and the case of a spherical particle is described below in this section.

The extinction cross section gives all the light removed from the incident beam, scattered *and* absorbed. To get the formula for the extinction one has to apply the optical theorem [11]. The basic concept of this is to take into consideration that the incident plane wave (u_0) and the outgoing spherical wave (u) (similar to the equations 2.17 and 2.18) is superposed coherently in the forward direction. To capture the forward intensity one can imagine a sensor with a finite size in the x-, y-plane at a very large distance z from the scatterer. All values of x and y within the plane of the sensor is $\ll z$. The radius at the sensor in the limit $z \to \infty$ is $r = z + (x^2 + y^2)/2z$ and the scattering amplitude $S(\varphi, \theta) \to S(0)$. In this limit the superposition of the incident and scattered wave is [11]:

$$u_0 + u = u_0\{1 + \frac{S(0)}{ikz} e^{-ik(x^2+y^2)/2z}\} \tag{2.20}$$

By squaring the magnitude of this expression 2.20, one gets the intensity, and by integrating this intensity over the area of the sensor (The sensor needs to be large enough to collect all the forward directed light). The integral gives the result $O - C$, where O is the area of the sensor and C is the area that has effectively been covered up by the particle. The term C is the general extinction cross section, which from now is termed C_{ext}, and is defined by [11]:

$$C_{ext} = \frac{4\pi}{k^2} Re\{S(0)\} \tag{2.21}$$

The principle of conservation of energy now states the formula [11]:

$$C_{ext} = C_{sca} + C_{abs} \tag{2.22}$$

Where C_{abs} is the absorption cross section, describing the effective area covered up in the incident beam to account for the absorbed light. From the $C´$s in 2.22 we can define the efficiency factors independent of the size of the sphere, by dividing on the geometrical cross section of the sphere, G [11]:

$$\frac{C_{ext}}{G} = \frac{C_{abs}}{G} + \frac{C_{sca}}{G} \Rightarrow Q_{ext} = Q_{abs} + Q_{sca} \tag{2.23}$$

Where the $Q´$s are the corresponding efficiency factors and $G = \pi a^2$, the cross section with radius a.

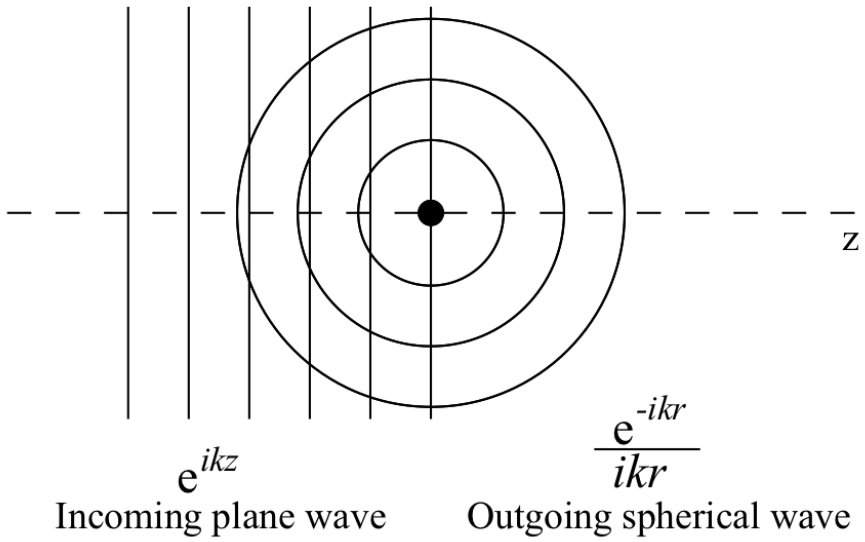

Figure 2.3: The incoming plane wave is shown as the straight lines, representing wavefronts, perpendicular to the z-axis. The outgoing spherical wave representing the scattered wave is shown as the concentric circular wavefronts. in the figure k is the wavenumber and r is the distance from the centre of the spherical wave.

For a spherical particle the amplitude functions $S_3 = S_4 = 0$, hence the electrical components may be written [11]:

$$E_\perp = S_1(\theta)\frac{e^{-ikr+ikz}}{ikr}E_{0\perp} \tag{2.24}$$

$$E_{\parallel} = S_2(\theta)\frac{e^{-ikr+ikz}}{ikr}E_{0\parallel} \tag{2.25}$$

Where k is the wavenumber and z the distance along the z-axis, r the radius from the centre of the spherical wave, $E_{0\perp}$ is the electrical component of the incident wave perpendicular to the scattering plane and $E_{0\parallel}$ is the electrical component of the incident wave parallel to the scattering plane.

The intensity of scattered unpolarized light is given as [11]:

$$I(\theta) = \frac{1/2(i_1 + i_2)}{k^2 r^2} I_0, \tag{2.26}$$

where

$$i_1 = |S_1(\theta)|^2, \quad i_2 = |S_2(\theta)|^2, \tag{2.27}$$

I_0 the intensity of the incident light and r is the distance from the centre of the sphere. The function $F(\theta, \varphi)$ from eq. 2.19, will in the case of a spherical scatterer be $F(\theta) = 1/2(i_1 + i_2)$. For polarized light only one of the i's are needed. For perpendicular polarized light $i_2 = 0$, and for parallel polarized light $i_1 = 0$, which corresponds to the function $F(\theta) = i_1$ and $F(\theta) = i_2$.

2.4 Mie scattering theory for spheres of arbitrary size

In this section the formulas for the extinction cross section and efficiency for the Mie theory is presented. The formuls for the amplitude functions are presented in the next section (sec. 2.4.1).

The Mie scattering theory is a rigorous mathematical theory describing the problem of light scattering by a sphere of arbitrary size and refractive index. This involves a formal solution of Maxwell's equations with proper boundary conditions. From Maxwell's equations, the scalar wave equation (given in appendix A.4, eq. A.20) can be derived. The incoming plane wave and the outgoing spherical wave, shown in fig. 2.3, are examples of solutions that satisfy the wave equation.

The field on the outside of the scattering sphere equals the incoming plane wave plus the outgoing scattered wave. The solution to the scattering problem needs to take into consideration that the field outside of the boundary is consistent with the field inside of the boundary, as stated by the boundary conditions.

Expressions for incoming, outgoing and inside wave in spherical coordinates are given in appendix A.1.1. These are wave functions constructed to be consistent with the boundary conditions and are solutions to the wave equation. The wave function for the scattered wave has the coefficients a_n and b_n and the inside wave has the

coefficients c_n and d_n. These coefficients are determined by taking the boundary conditions into consideration. The coefficients for the scattered wave are important for the scattering amplitude, and are given in section 2.4.1 (eqs. 2.32 and 2.33). The coefficients c_n and d_n for the inside wave are important when calculating the absorption explicitly from the inside electrical field, and are given in appendix A.1 (eqs. A.3 and A.4)

2.4.1 The amplitude functions

The amplitude functions $S_1(\theta)$ and $S_2(\theta)$ are given by the formulas [11]:

$$S_1(\theta) = \sum_{n=1}^{\infty} \frac{2n+1}{n(n+1)} \{a_n \pi_n + b_n \tau_n\} \tag{2.28}$$

$$S_2(\theta) = \sum_{n=1}^{\infty} \frac{2n+1}{n(n+1)} \{b_n \pi_n + a_n \tau_n\} \tag{2.29}$$

Where π_n and τ_n are functions of $\cos\theta$ given by:

$$\pi_n(\cos\theta) = \frac{1}{\sin\theta} P_n^1(\cos\theta) \tag{2.30}$$

$$\tau_n(\cos\theta) = \frac{d}{d\theta} P_n^1(\cos\theta) \tag{2.31}$$

The term $P_n^1(\cos\theta)$ is an associated Legendre polynomial and is given fully in appendix A.1.1. The coefficients a_n and b_n in the amplitude functions are given as [11]:

$$a_n = \frac{\psi_n'(y)\psi_n(x) - m\psi_n(y)\psi_n'(x)}{\psi_n'(y)\zeta_n(x) - m\psi_n(y)\zeta_n'(x)} \tag{2.32}$$

$$b_n = \frac{m\psi_n'(y)\psi_n(x) - \psi_n(y)\psi_n'(x)}{m\psi_n'(y)\zeta_n(x) - \psi_n(y)\zeta_n'(x)} \tag{2.33}$$

The function $\psi(z)$ of x or y are spherical Bessel functions multiplied by x or y respectively (replacing z) and $\psi'(z)$ is the derivative of this function. [11]:

$$\psi_n = z j_n(z) \tag{2.34}$$

The function $\zeta_n(x)$ is given by:

$$\zeta_n(x) = x h_n^{(2)}(x) \tag{2.35}$$

The function $h_n^{(2)}(x)$ is the third kind of Bessel function, called the Hänkel function, and is given in appendix A.3. The variables x and y are given as $x = ka$ and

$y = mka$ [11], where k is the wavenumber, a is the radius of the sphere, and m is the complex refractive index ($m = n + in'$).

The amplitude functions needs to be calculated numerically, and are done so by MATLAB functions developed by Mätzler [19]. Calculation of the exact Mie solution is discussed in section 3.1.

2.4.2 Mie efficiency factors

For forward Mie scattering, the amplitude functions $S_1(0) = S_2(0) = S(0)$. The extinction efficiency factor is found by dividing the general extinction cross section defined in equation 2.21 by the geometrical cross section $G = \pi a^2$:

$$Q_{ext} = \frac{4}{k^2 a^2} Re\{S(0)\}, \tag{2.36}$$

where k is the wavenumber and a is the radius of the sphere. The scattering efficiency factor is given by [11]:

$$Q_{sca} = \frac{1}{k^2 a^2} \int_0^\pi \{i_1(\theta) + i_2(\theta)\} \sin\theta d\theta, \tag{2.37}$$

where θ is the scattering angle, i_1 and i_2 is the perpendicular and parallel component of the intensity relative to the scattering plane (eq. 2.27). The extinction cross section is defined in the forward direction and includes the chemical absorption of electromagnetic radiation in the sphere. It represent all lost radiation in the forward direction. The scattered part of the extinction can be recovered by integrating the intensity of the light over a spherical shell enclosing the whole sphere. As implied from eq. 2.22, the radiation still not accounted for, is absorbed by the sphere. Thus the absorption efficiency can implicitly be written:

$$Q_{abs} = Q_{ext} - Q_{sca} \tag{2.38}$$

The next section will show how to calculate the absorption efficiency explicitly by taking the inside field of the sphere into account.

2.4.3 Absorption efficiency

The absorption efficiency curve can be calculated explicitly by taking the averaged internal electrical field $\langle|\mathbf{E}|^2\rangle$ into consideration. The formula for Q_{abs} is derived from the formula for the absorption cross section given by Ishimaru [20], who states the formula as [20]:

$$C_{abs} = \int_V k\varepsilon''(r')|\mathbf{E}(r')|^2 dV' \tag{2.39}$$

With an homogeneous material $\varepsilon''(r') \to \varepsilon''$. By replacing the squared magnitude of the electrical field $|\mathbf{E}(r')|^2$ with the electrical field squared over a spherical shell (all φ and θ, constant r') $\langle|\mathbf{E}|^2\rangle$, and expressing the volume integral in spherical coordinates, the integral over the spherical shell may be taken leaving the factor 4π. The absorption efficiency is now obtained by assuming the incident electrical field amplitude is unitary ($|E_i| = 1$) [20], and by doing the change of variable $r'k \to x'$ and dividing by the geometrical cross section $G = \pi a^2$ [19]:

$$Q_{abs} = \frac{4\varepsilon''}{x^2} \int_0^x \langle|\mathbf{E}|^2\rangle x'^2 dx', \tag{2.40}$$

were ε'' is the imaginary part of the complex dielectric constant $\tilde{\varepsilon}_r$, x is the size parameter and $x' = r'k$, with r' giving the distance from the centre of the sphere ($0 < r' < a$).

The averaged internal field at at the radius r' is given by [19]:

$$\langle|\mathbf{E}|^2\rangle = \frac{1}{4} \sum_{n=1}^{\infty} \left(m_n|c_n|^2 + n_n|d_n|^2\right) \tag{2.41}$$

The coefficients c_n and d_n are given in appendix A.1, and are the internal equivalents of the Mie scattering coefficients a_n and b_n. The coefficients m_n and n_n (appendix A.1) are the scalar values of the vector-wave harmonic field $\mathbf{M}_{oln}^{(1)}$ and $\mathbf{N}_{eln}^{(1)}$, which is discussed later (section 4.1). A MATLAB-function has been developed for calculating Q_{abs} by C. Mätzler [19].

2.5 Infrared microspectroscopy

In Fourier transform infrared microspectroscopy (FTIRM), the well known technology of the Fourier transform infrared (FTIR-) spectrometer [6], is combined with the focusing optics similar to a light microscope. The purpose of FTIRM is being able to obtain infrared spectra from microscopic sized samples, or to examine details of a larger inhomogeneous sample with a spatial resolution near the diffraction limit (sec. 2.5.1). This increases the range of applications of FTIR-spectroscopy to i.a. biological tissue and cells.

The general principle of FTIR-spectroscopy is to send a beam of light through a sample and detecting the transmitted light. Before passing through the sample the beam of light needs to be subjected to a Michelson interferometer which creates wavelength-dependent interference in the beam. This is done by splitting the beam and reuniting it with a phase difference determined by a movable mirror. The interference effect

repress different wavelengths for different phase differences, creating a signal at the detector which is a superposition of all the wavelengths in the beam. Wavelengths of absorbed light will contribute less to the signal. When the signal created by the detector is Fourier transformed, the spectra appear in form of wavenumber dependent intensity. The raw spectra are scaled against a reference spectrum to remove absorptions from the ambient medium and to make the spectra independent of the source spectrum. The remaining spectrum is defined as the transmission T [6, 16]:

$$T = \frac{I}{I_0} \tag{2.42}$$

Where I is the intensity of the sample spectra and I_0 is the intensity of the reference spectrum (the incident light). From this we can define the absorbance [16]:

$$A = -log_{10}(T) \tag{2.43}$$

The equation 2.43 is equivalent with Beer-Lambert's law stating a linear relationship between the concentration of an infrared active functional group C $[mol/L]$ the extinction coefficient ε $[10^3 L/(mol\ cm)]$ and the path length l $[cm]$ of the incident light in the medium. From this relationship the absorbance is stated as [5]:

$$A = \varepsilon C l \tag{2.44}$$

2.5.1 Focusing optics

In infrared microspectroscopy the focusing optics usually is a Schwartzschild objective, put on each side of the sample, each of them creating a focal point in the plane of the sample as shown in figure 2.4. The range of angles focused into the focal plane is given by the numerical aperture (NA) of the objective, and is defined by:

$$\mathrm{NA} = n \sin \theta_{\mathrm{NA}} \tag{2.45}$$

where n is the refractive index of the ambient medium ($\simeq 1.0$ in air), and θ_{NA} is the largest angle covered by the objective. A usual value for the NA of an infrared microscope is ~ 0.60, which correspond to a range of $\theta \in [-37^o, 37^o]$ [21].

The diffraction-limited spatial resolution of the infrared microscope is dependent on the wavelength of the light and the NA of the focusing optics. Apertures are often used to limit the area of the beam to the sample's region of interest, which can be seen in fig. 2.4. With a single aperture before the sample the diffraction-limited resolution is about $2\lambda/3$, or between $1.7\mu m$ and $13\mu m$ in the mid-IR range. To further improve the spatial resolution, a second aperture is in some cases put after the sample to

control the area of the beam reaching the sensor (shown in fig. 2.4). This improves the spatial resolution to $\sim \lambda/2$. [21]

The definition of transmission in equation 2.42 will in terms of the extinction be defined as [16]:

$$T = 1 - Q_{ext} \tag{2.46}$$

In the forward direction the equation 2.23 states that the extinction efficiency is $Q_{ext} = Q_{sca} + Q_{abs}$. With a numerical aperture some of the scattered light collected by the focusing objective and directed towards the sensor. The term Q_{sca} becomes smaller, and therefore we need to define a new term Q_{NA} which is the efficiency of the objective collecting the scattered light:

$$Q_{\mathrm{NA}} = \frac{1}{x^2} \int_0^{\theta_{\mathrm{NA}}} \{i_1(\theta) + i_2(\theta)\} \sin\theta d\theta \tag{2.47}$$

Where θ_{NA} is the largest angle of which scattered light will be collected by the objective, x is the size parameter, and i_1 and i_2 is the intensity components of the scattered light (eq. 2.27).

We can now define a new scattering efficiency $Q_{sca,\mathrm{NA}}$ which include light scattered at larger angles than θ_{NA}:

$$Q_{sca,\mathrm{NA}} = Q_{sca} - Q_{\mathrm{NA}} \tag{2.48}$$

The extinction efficiency term Q_{ext} also needs to be redefined to exclude the light collected by the focusing objective. The new extinction efficiency $Q_{ext,\mathrm{NA}}$ can be defined:

$$Q_{ext,\mathrm{NA}} = Q_{ext} - Q_{\mathrm{NA}} \tag{2.49}$$

The equation 2.49 gives the extinction when using a infrared spectrometer with a microscope. The transmission measured is given by equation 2.46 where Q_{ext} is replaced by $Q_{ext,\mathrm{NA}}$.

2.5.2 Synchrotron radiation source

In infrared microspectroscopy, a synchrotron light source is often used instead of a more traditional thermal IR-source to produce a more readable absorption spectrum. A synchrotron is an electron storage ring, which produces a broad spectrum (from x-ray to far-infrared) of light. Synchrotron radiation is emitted when the electrons is accelerated by the bending magnets in the ring, creating a narrow angular distribution dependent on the wavelength of the light, and the radius of the bending motion. A selected spectral range can be collected from the synchrotron by adjusting the opening angle [7, 21]

The advantage of a synchrotron light source compared to a more conventional thermal source is that the synchrotron source is 100-1000 times brighter. This is because the light comes from a small effective source and is emitted in a narrow range of angles. The high flux density is especially an advantage when dealing with small aperture sizes; since it allows small regions of the IR-sensor to be exposed to more radiation, the detected signal is less noisy (lower signal to noise ratio). The advantage of the synchrotron light source vanishes when the aperture size is above 70 μm. [21]

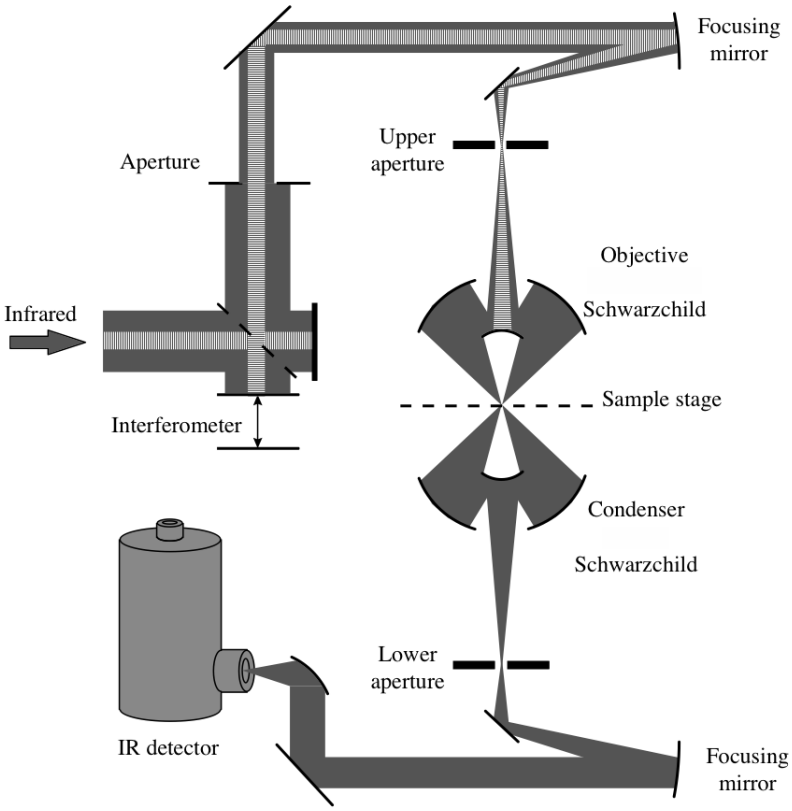

Figure 2.4: Schematic drawing of an IR-microscope showing where the infrared light from the synchrotron enters, the Schwarzschild objects and apertures over and under the sample plane. Reprinted by courtesy of Paul Dumas [21]

.

3 Exact Mie scattering and approximations to the Mie solution

In the forward and non-forward direction the coefficients π_n and τ_n needs to be calculated by recurrence relations, which is computationally intensive. By modern computers, the exact solutions are achievable, but slow when they need to be calculated repeatedly. Approximation formulas thus present an attractive alternative to the exact solution in many situations [9, 10]. Approximation formulas are also often easier to interpret for example in terms of optical rays. Exact calculations by integrating over angles make calculations even more intensive. Further, the approximation formulas also facilitate solving the "inverse" problem, where the size and shape of an unknown particle or particle distribution is described using the scattering patterns.

3.1 Computation of exact efficiency curves

To calculate the efficiency curves using the exact Mie theory, computer codes is required that can estimate the infinite sums of the amplitude functions $S_1(\theta)$ and $S_2(\theta)$ (eq. 2.28 and 2.29). The amplitude functions contain Legendre polynomials (in equations 2.30 and 2.31) that contain sums with an increasing number of terms as the summation index n increases. The Bessel functions also contain infinite sums which need to be calculated for each term in the the amplitude functions.

C. Mätzler [19] has developed MATLAB code for the computation of the Mie coefficients and and efficiencies. This code is based on the proposed algorithm to calculate the exact Mie solution given in Bohren and Huffman [18].

Mätzler also follows the algorithm suggested by Bohren and Huffman to overcome computational difficulties. For example Bohren and Huffman suggest the maximum number of terms $n = n_{max}$ in the sum of eqs. 2.28 and 2.29 and when calculating

the forward efficiency directly from the Mie coefficients a_n and b_n. The formula for n_{max} is [19]:

$$n_{max} = x + 4x^{1/3} + 2 \tag{3.1}$$

where x is the size parameter, and n_{max} is rounded off to the closest integral.

The algorithm used for calculating the Bessel functions are MATLAB's built in functions for all but the zeroth and first order. These are given in their expanded forms. The functions $\pi_n(\cos\theta)$ and $\tau_n(\cos\theta)$ are calculated from the recurrence relations [18]:

$$\pi_n = \frac{2n-1}{n-1}\mu\pi_{n-1} - \frac{n}{n-1}\pi_{n-2} \tag{3.2}$$

and

$$\tau_n = n\mu\pi_n - (n+1)\pi_{n-1}, \tag{3.3}$$

where $\mu = \cos\theta$, and the first terms of π_n are $\pi_0 = 0$ and $\pi_1 = 1$.

Mätzler includes a MATLAB function for calculating the absorption efficiency by the equation 2.40. This function requires the averaged electrical field inside the sphere, which is calculated at n_j points between 0 and $x = ka$. The number of points n_j is given by the formula [19]:

$$n_j = 5 \cdot (2 + x + 4x^{1/3}) + 160 \tag{3.4}$$

Where $x = ka$. The reason for this formula is not given [19].

To generate Mie extinction curves containing absorption bands, a complex refractive index is simulated by adding a set of absorption resonances to the real electric permittivity $\bar{\varepsilon}$ (eq. 2.13). The formula for describing the shape, location and magnitude of the absorption band is dependent on the complex permittivity, which is given by [16]:

$$\tilde{\varepsilon} = \bar{\varepsilon} + \sum_{j \epsilon IR} \frac{\Lambda_j}{\tilde{\nu}_j^2 - \tilde{\nu}^2 - i\Gamma_j\tilde{\nu}} \tag{3.5}$$

Where Λ_j is a parameter describing the strength of the j-th absorption band, Γ_j is a parameter describing the width of the j-th absorption band, $\tilde{\nu}_j$ is the wave number of the j-th absorption band and $\tilde{\nu}$ is the wavenumber of the infrared light. An example of where this is done is the program in appendix B.1, which calculates extinction, scattering and absorption by applying Mätzler's MATLAB functions. The coefficients of 3.5 are given as a matrix, which generate the complex refractive index for each wavenumber k the scattering, extinction and absorption is calculated for. Equation 3.5 is equivalent with equation 2.12, but the factors describes the absorption bands more qualitatively since information of mass and charge of each type of dipole is hard to acquire in practice [16].

The complex permittivity is related to the refractive index by $m = \sqrt{\tilde{\varepsilon}}$ (eq. 2.14). In this example, absorption bands were added at the wave numbers $1650cm^{-1}$, $2500cm^{-1}$ and $2650cm^{-1}$.

In figure 3.1 a MATLAB-function for calculation of forward scattering has been used to create the extinction efficiency curve and a forward scattering efficiency curve. The absorption curve is calculated by subtracting the scattering curve from the extinction curve.

Figure 3.2 shows $T = 1 - Q_{ext,\mathrm{NA}}$, where $Q_{ext,\mathrm{NA}}$ is given in equation 2.49, with an increasing value of NA, meaning that the amount of scattered light which does not reach the sensor decreases. The figure shows that when θ_{NA} goes to 180^o, only the absorption efficiency Q_{abs} is left. The intensity functions $i_1(\theta)$ and $i_2(\theta)$, for perpendicular and parallel intensity, is calculated using Mätzler's MATLAB functions [19] for amplitude functions $S_1(\theta)$ and $S_2(\theta)$. These functions are integrated, using equation 3.2, over the range of θ in question with a step size $\Delta\theta = 1^o$. The extinction efficiency factor Q_{ext} is calculated using Mätzler's functions [19].

Figure 3.2 **b** shows the transmissivity $T = 1 - Q_{ext}$ where no scattering is present, giving $T = 1 - Q_{abs}$. The absorption bands is in the same place in both plots and of the same height as the red line in figure 3.2. The absorption efficiency Q_{abs} in figure 3.2 **a** is calculated by Mätzler's formula based on equation 2.40. This figure shows that the Mätzler's functions for calculating the absorption efficiency, the forward extinction and amplitude functions $S_i(\theta)$ is consistent with the definition $Q_{ext} = Q_{abs} + Q_{sca}$, since $T = 1 - Q_{ext,\mathrm{NA}}$ and $T \to 1 - Q_{abs}$ when $\theta_{\mathrm{NA}} \to 180^o$.

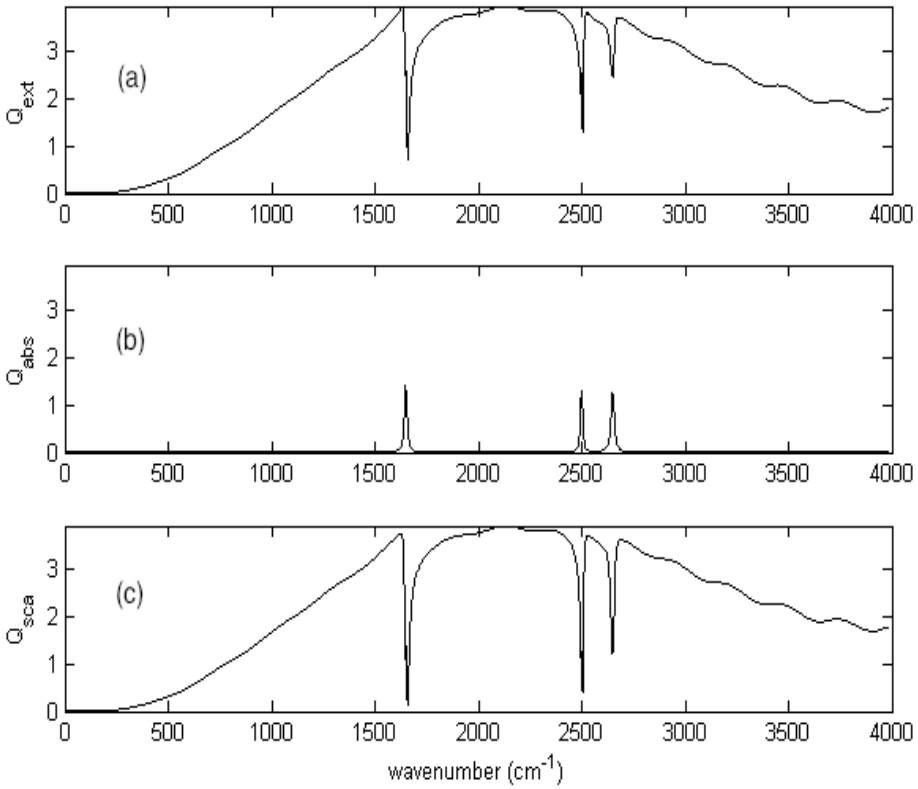

Figure 3.1: **a**: The extinction efficiency Q_{ext} curve for a sphere with diameter $a = 5\mu m$ and refractive index $Re(m) = 1.3$. **b**: The absorption efficiency curve Q_{abs} for a sphere with diameter $a = 5\mu m$ and refractive index $Re(m) = 1.3$. **c**: The scattering efficiency curve Q_{sca} for a sphere with diameter $a = 5\mu m$ and refractive index $Re(m) = 1.3$. The wave numbers on the x-axis are $\tilde{\nu} = 1/\lambda$ $[cm^{-1}]$.

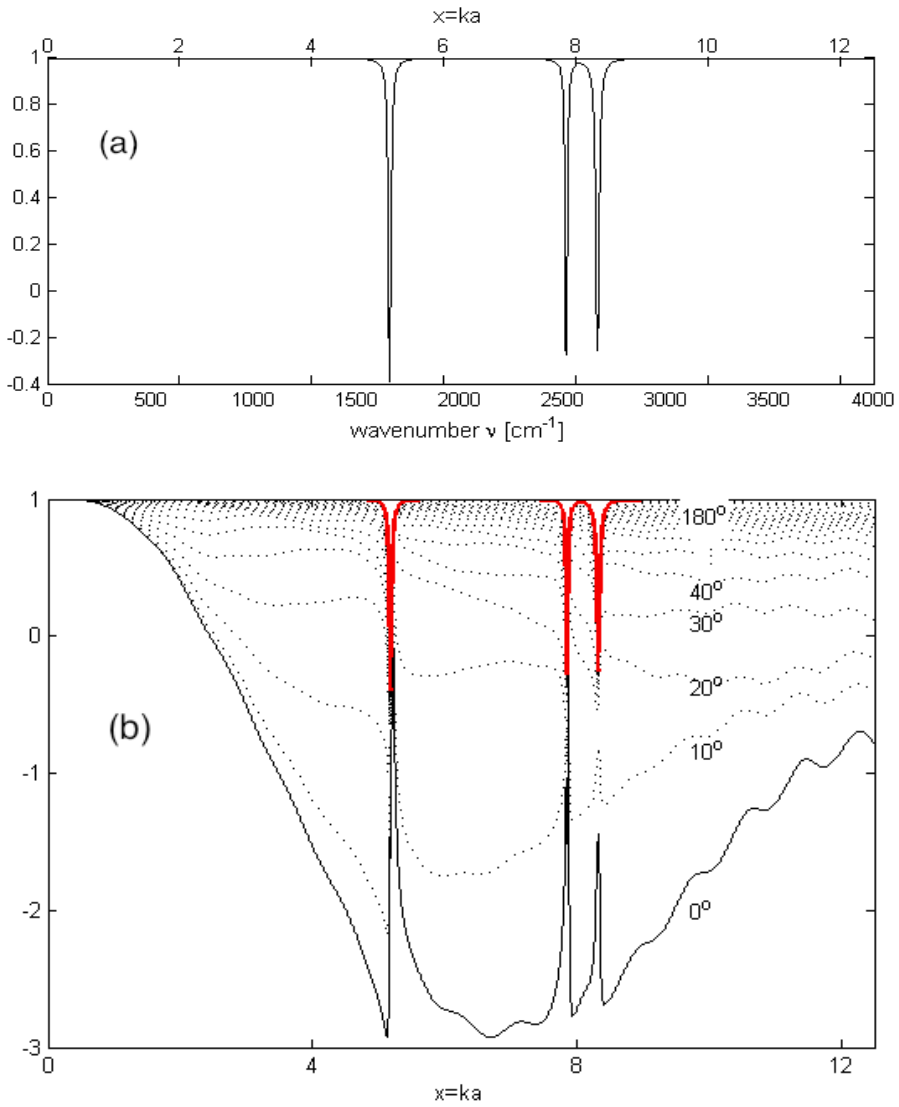

Figure 3.2: The sphere used in the calculation has the radius $5\mu m$ and the range of wavenumber $\tilde{\nu}$ is from 0 cm^{-1} to 4000 cm^{-1}. This correspond to the range of size parameter $x = 2\pi\tilde{\nu}a$ of 0 to 12.5. The refractive index for both calculations are $m = 1.3$. **a**: The curve of $T = 1 - Q_{abs}$, where Q_{abs} is calculated by Mätzler's function based in the internal electrical field (eq. 2.40). **b**: The solid black curve shows $T = 1 - Q_{ext,\mathrm{NA}}$ with NA corresponding to an angle $\theta_{\mathrm{NA}} = 0^o$. The dotted curves show T with an increasing value of NA corresponding to $\theta_{\mathrm{NA}} = 10^o, 20^o, ..., 170^o$. The solid red curve is T calculated with $\theta_{\mathrm{NA}} = 180^o$, showing $T = 1 - Q_{abs}$.

3.2 Approximation of efficiency curves in forward direction

The Mie formulas in the forward direction is much simpler than in the non-forward direction. When $\theta = 0$, the coefficients $\pi(\cos\theta)$ and $\tau(\cos\theta)$ becomes $\pi(1) = \tau(1) = \frac{1}{2}n(n-1)$, making the formula for

$$S(0) = \frac{1}{2}\sum_{n=1}^{\infty}(2n+1)(a_n + b_n) \tag{3.6}$$

The exact scattering efficiency Q_{ext} can also be calculated by the coefficients a_n and b_n by applying the optical theorem, similar to what is done for C_{ext} (eq. 2.21) in section 2.3.1 [11]:

$$Q_{sca} = \frac{2}{x^2}\sum_{n=1}^{\infty}(2n+1)\mathrm{Re}\{a_n + b_n\} \tag{3.7}$$

Still the calculations are computationally heavy and non-intuitive which makes approximations to the scattering problem useful.

3.2.1 Anomalous diffraction approximation (ADA)

The approximation made by van de Hulst [11] for the extinction efficiency factor Q_{ext}, is done under the assumptions that the refractive index m is close but not equal to 1, and $x = ka$ is large. The assumptions describes scattering in the anomalous diffraction domain, which disregards refraction and reflection ($m \simeq 1$), and therefore views transmitted rays as straight lines. This means that the scattered intensity is concentrated close to the original direction of propagation. The light traveling trough the sphere suffers, even though not undergoing significant refraction, a significant phase lag. This light will constructively and destructively interfere with the light diffracted as from a circular disk, with the area equal to the geometrical cross section of the sphere. The field in the shadow of the sphere is $e^{-i\rho\sin\tau}$ given a field of magnitude 1 outside the shadow, where τ is the angle relative to the tangent of the sphere at the point the ray hits the sphere, and $\rho = 2x(m-1)$ describes the phase lag of the ray going through the centre of the sphere ($\tau = 90^o$). The scattered field adds the factor $e^{-i\rho} - 1$ to the original field in the forward direction. To find the scattering amplitude $S(0)$, Babinet's principle is applied, since the scattered and the remaining field adds to the original field.

Babinet's principle tells us that the diffraction pattern for a circular hole is the same as the on of a circular opaque disc with the same radius. The disturbances in the

plane wave caused by the diffraction pattern from the circular hole and the disk of the same size, are equal in amount but opposite in sign [11]. Since the diffracted field that is *added* to the field inside the shadow of the sphere is $(e^{-i\rho\sin\tau}-1)$, the scattered wave must be the same, but with opposite sign, assuming that Babinet's principle can be applied. Thus yielding the scattered wave $(1-e^{-i\rho\sin\tau})$. The amplitude in forward direction is:

$$S(0) = k^2a^2\int_0^{\pi/2}(1-e^{-i\rho\sin\tau})\cos\tau\sin\tau\ d\tau \tag{3.8}$$

Where the integral is taken over the whole geometrical shadow and τ is the angle relative to the tangent of the sphere. The Mie extinction efficiency curve is calculated from the real part of $S(0)$ (eq. 2.36). By performing the integration and setting $ka = x$, the amplitude function becomes:

$$S(0) = x^2\left[\frac{1}{2}+\frac{e^{-i\rho}}{i\rho}+\frac{e^{-i\rho}-1}{(i\rho)^2}\right] \tag{3.9}$$

This gives by equation 2.36 the approximate extinction efficiency curve when we assume a real refractive index m:

$$Q_{ext} = 2-\frac{4}{\rho}\sin\rho+\frac{4}{\rho^2}(1-\cos\rho) \tag{3.10}$$

where $\rho = 2x(m-1)$. This is a widely used function for calculating approximate Mie contribution to scattering by spherically shaped particles [2, 5, 10] . Figure 3.3 shows the function 3.10 plotted against the exact Mie solution.

For the case when the refractive index is a complex number i.e. when absorption resonances are present in the spectral range of the incident light, the approximation is:

$$\begin{aligned} Q_{ext} = 2 &- 4e^{-\rho\tan\beta}\frac{\cos\beta}{\rho}\sin(\rho-\beta) \\ &- 4e^{-\rho\tan\beta}\left(\frac{\cos\beta}{\rho}\right)^2\cos(\rho-2\beta)+4\left(\frac{\cos\beta}{\rho}\right)^2\cos 2\beta \end{aligned} \tag{3.11}$$

Where $\tan\beta = \frac{n'}{n-1}$ and $m = n-in'$

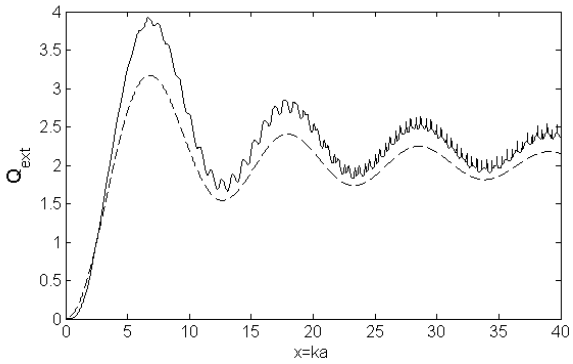

Figure 3.3: The curves show Q_{ext} calculated by eq. 3.10 plotted against the size parameter. The striped curve is made by using the anomalous diffraction approximation, while the solid curve is the exact Mie solution.

3.2.2 Approximation for $x \to 0$; a comparison of Blümel´s and Wiscombe´s approximation

In an article by Wiscombe [12] the author presents an algorithm for the approximation of Mie scattering when the size parameter $x \to 0$. The purpose of this work was to make fast efficient computer codes for estimating the scattering with a high degree of accuracy. Considering the much higher capacity of todays computers, this was first of all a problem at the time Wiscombe´s article was written. The approximations of the extinction and scattering efficiency are given as:

$$Q_{ext} = 6x \text{ Re}\left(\hat{a}_1 + \hat{b}_1 + \frac{5}{2}\hat{a}_2\right) \tag{3.12}$$

And:

$$Q_{sca} = 6x^4 T \tag{3.13}$$

The formulas for $\hat{a}_1$, $\hat{a}_2$, $\hat{b}_1$ and T are given in appendix A.5. The formulas require a complex refractive index m.

The author claims that the approximation has an accuracy of 2-3 digits up to $x = 0.5$, with increasing accuracy for lower values of x. The complex refractive index must have an absolute value lower or equal to 2. Wiscombe also include formulas for calculating $S_1(\cos\theta)$ and $S_2(\cos\theta)$. These are not tested in this work, but are given in appendix A.5.

Blümel´s approximation [13] for $x \to 0$ is based on the assumption that for small values of x only $n = 1$ contributes significantly to the sum in Q_{sca} by equation 3.7.

Therefore only the $n = 1$ term is kept from the sum. The sum is then expanded as a power series of x. The functions a_n (eq. 2.32) and b_n (eq. 2.33) are evaluated for $n = 1$ to the leading order in x; only the a_1 term contributes to Q_{ext} for $x \to 0$. The extinction efficiency factor for a complex refractive index becomes:

$$Q_{ext}(x) = \frac{6}{x^2} \frac{\mathrm{Re}(ND*)}{|D|^2} \tag{3.14}$$

Where $m = n + in'$ is a complex number, $N = x^3(1 - m^2)$ and $D = x^3(1 - m^2) + \frac{3}{2}i(2 + m^2)$.

In figure 3.4 the two approximations are compared to the exact Mie solution. Absorption bands are added to the dielectric constant to make a complex refractive index. The absorption bands are located the same places as in section 3.1, which in the case of $a \sim 10\mu m$ sphere is out of range in figure 3.4. Both of the approximations seem to converge towards the exact solution at low values of x, but Blümel's formula converges towards zero for a larger value of x than Wiscombe's formula, thus giving a slightly larger range of validity. If the approximations are plotted for lower values of $Re(m)$, one can see that Blümel's formula will overestimate the scattering for values of x before converging towards zero. In fig 3.4 the approximations and the exact solution are plotted on a logarithmic scale. This shows that for $x \to 0$ Blümel's formula coincides with the exact solution, while Wiscombe's formula differs slightly.

In figure 3.5 the relative error in the approximations is plotted. The relative errors are calculated by the formula:

$$\varepsilon_{rel}(x) = \frac{Q_{ext,Mie}(x) - Q_{ext,Approx}(x)}{Q_{ext,Mie}(x)} \tag{3.15}$$

where $Q_{ext,Mie}$ is the efficiency factor calculated by the Mie solution, while $Q_{ext,Approx}$ is either Wiscombe's or Blümel's approximation. The plots in fig. 3.5 show that Blümel's approximation converges towards the exact solution with $\epsilon_{rel} \to 0$ when $x \to 0$, while the relative error of Wiscombe's approximation diverges when x goes lower than about 0.02, and levels of at a relative error of about 2. It can be shown (derivation in appendix A.5.1) that the relative difference for Wiscombe's approximation when $x \to 0$ becomes:

$$\lim_{x \to 0} \varepsilon_{rel} = 1 + \frac{A + 2(nn')^2}{A - 2(nn')^2 + 4nn'} \tag{3.16}$$

where $n = Re(m)$, $n' = Im(m)$ and $A = 4 + 4n^2 - 4n'^2 + n^4 + n'^4$.

If $nn' < 1$, then $\lim_{x \to 0} \varepsilon_{rel} < 2$. Because of the constant 4 in A and since A includes the leading powers of n an n', the relative difference will be $\simeq 2$ for m. The

expression 3.16 is actually the relative difference between Blümel's and Wiscombe's approximation, but this works under the assumption that Blümel's approximation is exact in the limit $x \to 0$, which it proves to be in the log-log-plot in figure 3.4 **b** and in the small-x relative error plot in figure 3.5.

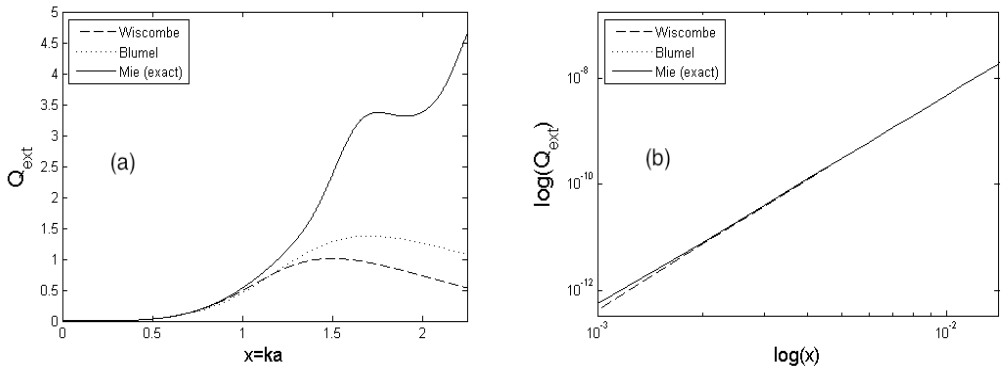

Figure 3.4: **a**: Wiscombe's and Blumel's approximation compared to the exact solution, plotted with complex refractive index ($Re(m) \sim 1.8$). **b**: Log-log plot of Wiscombe's and Blümel's approximation compared to exact solution. The imaginary part is determined by absorption bands outside the region investigated in these plots and is assumed to be $\ll 1$.

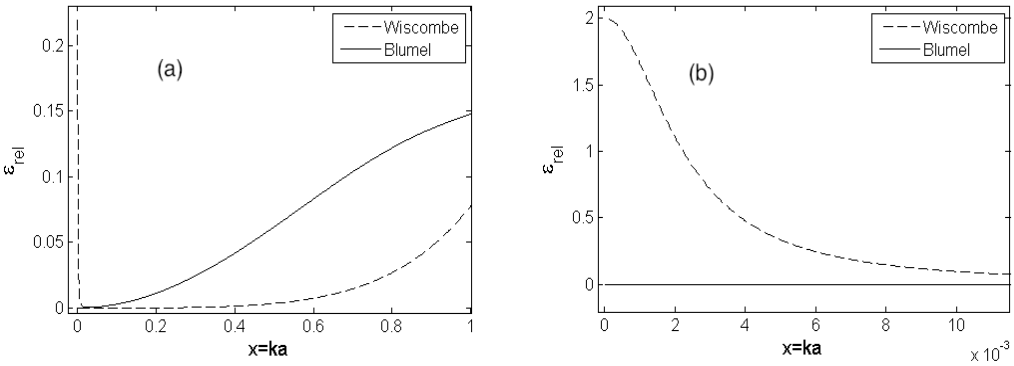

Figure 3.5: **a**: The relative difference between the approximation and the exact solution for a wider range of x than plot **a**. **b**: The relative difference between the approximation and the exact solution for $x \to 0$. In both **a** and **b** the real part of the refractive index ($Re(m) \simeq 1.8$). The imaginary part of the refractive index is assumed to be $\ll 1$.

3.3 Approximation of efficiency curves in non-forward direction

The approximations presented in this section are all based on modeling the intensity at an angle θ after the forward solution, meaning that the exact solution is in fact used, but the intensity at an angle θ is approximated by scaling the forward solution.

3.3.1 Penndorf-Shifrin-Punina/Fymat-Mease (PSP/FM-) Approximation

The PSP/FM-approximation is a method for calculating the intensity of scattered light at different angels θ. The method is based on the approximation formula for forward scattering intensity derived by Penndorf [22]:

$$I_P = \frac{x^4}{4k^2}\left(\frac{Q_{ext}}{2}\right)^2 \tag{3.17}$$

Where the factors x, k and Q_{ext} are as defined previously. The approximation of angular intensities is based on the idea that the Fraunhofer's diffraction pattern has about the same shape in the vicinity of the forward direction as the full Mie solution [14]. By adjusting the Fraunhofer approximation to Mie scattering, the approximation can be applicable to values of the size parameter x down to $x \sim 1$. The Fraunhofer intensity at $\theta = 0$ is $I_F(0) = x^2/4k^2$, thus the Penndorf formula can be written as:

$$I_P(0) = I_F(0)\left(\frac{Q_{ext}}{2}\right)^2 \tag{3.18}$$

Equation 2.36 gives the formula for Q_{ext} in terms of the real part of $S(0)$. However, the intensity in the forward direction also includes the imaginary part (eq. 2.27). An assumption in this approximation is that $Re\{S(0)\} \gg Im\{S(0)\}$.

The Fraunhofer formula for arbitrary angle θ is [14]:

$$I_F(\theta) = \frac{x^2 J_1^2(x\sin\theta)}{k^2\sin^2\theta} \tag{3.19}$$

Where $J_1(x\sin\theta)$ is the first kind of Bessel function of 1. order, x is the size parameter and k is the wavenumber. Shifrin and Punina proposed to put the formula $I_F(\theta)$ (eq. 3.19) in place of the Fraunhofer formula for $\theta = 0$ which gives an estimation for the intensity for values of θ different from the forward direction. The Penndorf-Shifrin-Punina (PSP-) approximation formula is thus given as [14]:

$$I_{PSP}(\theta) = I_F(\theta)\left(\frac{Q_{ext}}{2}\right)^2 \tag{3.20}$$

Fymat and Mease proposes two functions f_1 and f_2 which are modeled taking into account the relative error between the real Mie solutions and the PSP-approximation. These functions are given as [14]:

$$f_1^{-1} \equiv f^{-1}[(m-1)x] = \begin{cases} 1 - J_0^2[(m-1)x], & \text{for } (m-1)x \leq a \\ & \text{or } b \leq (m-1)x \leq c \\ 1, & \text{otherwise} \end{cases} \tag{3.21}$$

$$f_2^{-1} \equiv f^{-1}[2(m-1)x] = \begin{cases} 1 - J_0^2[2(m-1)x], & \text{for } 2(m-1)x \leq d \\ 1, & \text{otherwise} \end{cases} \tag{3.22}$$

With a, b, c and d as constants for each value of refractive index. For a refractive index of $m = 1.33$ the constants are $a = 3.63$, $b = 5.52$, $c = 6.6$ and $d = 2.4$. This gives the Fymat and Mease (FM) approximation [14]:

$$I_{FM}(\theta) = I_{PSP}(\theta)\ f_1\ f_2 \tag{3.23}$$

The extension made by Fymat and Mease is based on the residual from the PSP-approximation, to increase the validity for low values of x. In their article [14], an improvement from the PSP-approximation is shown in the forward direction for different refractive indices.

3.3.2 Gordon-approximation

The Gordon approximation [15] is a method for estimating scattering of light by spheres. The approximation is based on an extension of the Rayleigh-Gans (or Rayleigh-Debye; R-D) approximation [1] made by Shimizu [23], which enters ma as the radius of the scattering sphere instead of only a. This allows the refractive index m to be included in the approximation, contrary to the unmodified R-D approximation. The formula for the intensity relative to the incident light is:

$$I(\theta) = I(0)[3 \cdot J_1(x_g)/x_g + \gamma(x_g)]^2[1 + \cos^2\theta]/2 \tag{3.24}$$

Where $J_1(x)$ is the Bessel function of first order, given in [15] as $J_1(x_g) = (\sin x_g - x_g \cos x_g)/x_g^2$ and $x_g = ka(1 + m^2 - 2m\cos\theta)^{1/2}$, with a and m as radius and refractive index of the sphere as usual. The subscript in x_g separates it from size

[1] Rayleigh-Gans scattering covers scattering by particles under the assumptions that the relative refractive index is close to 1, and that the phase shift is small, meaning that either the sphere is small or the change in refractive index is small compared to wavelength of the light. This means that the wave may pass through the particle without being refracted. A very small part of the wave is scattered in each volume element of the particle, and may pass through the other volume elements without being scattered further more. The scattered waves from the different volume elements in the same direction may interfere with each other because of different positions. The interference effects is the basis of Rayleigh-Gans scattering [11].

parameter $x = ka$ defined in van de Hulst [11]. In the unmodified R-D approximation, $x_g = 2ka\sin(\theta/2)$.

The forward intensity $I(0)$ is the relative intensity in the forward direction, and may be calculated by the scattering amplitude in the forward direction $S(0)$ from the exact Mie solution by [14]:

$$I(0) = k^{-2}\{(Re[S(0)])^2 + (Im[S(0)])^2\} \tag{3.25}$$

The function $\gamma(x_g)$ is included to ensure that the minima of $I(\theta) > 0$ when $J_1(x_g) = 0$. This function is non-analytical by definition [15], and may have different forms for different sized scatterers. Gordon proposes $\gamma(x_g) = x_g^{-3/2}$ and attributes it the same sign as $J_1(x_g)$, but acknowledges that more complicated forms of $\gamma(x_g)$ might give better approximations.

3.4 Solid angle integration by PSP, FM and Gordon's approximation

The Mie solutions to the scattering problem offers formulas for calculating the scattering efficiency Q_{sca} in the non-forward direction. When these formulas are used to integrate over a range of angles θ, the Mie solution needs to be calculated for each of the solid angles at each of the wave numbers in the spectrum. This is a computationally intensive process. Approximations that speeds up this process are therefore of interest.

The approximations made by Penndorf, Shifrin and Punina, modified by Fymat and Mease are presented in chap. 3.3.1. Plots of the intensity at different angles show that this approximation works best for angles in the vicinity of the forward direction. The plots of the intensities are shown in fig. 3.7. For small values of x the PSP/FM approximation works reasonably well even for angles up to (and above, though not shown in fig. 3.7) $\theta = 10^o$. For an increasing angle θ the approximation is less accurate for higher values of x. For example in the infrared spectroscopy of single cells of the size of 30 μm, x-values up to about 40 are required to cover the whole mid-IR region.

To get a better estimate of the scattering at larger angles θ than about 10, other approximations could be considered. The approximation by Gordon presented in section. 3.3.2, provides an estimate of the scattering intensity with better accuracy than the PSP/FM approximation at larger values of θ. This approximation does not give a good estimate at angles near the forward direction, as can be seen in the figure 3.6. The presence of the non-analytic modulating function $\gamma(x_g)$ provides the

opportunity to adjust the approximation to a certain range of validity. A combination of PSP/FM- and the Gordon approximation where used to obtain the scattering efficiency integrated from $\theta = 0^o$ to $\theta = \theta_{\mathrm{NA}}$ in section 3.4.1.

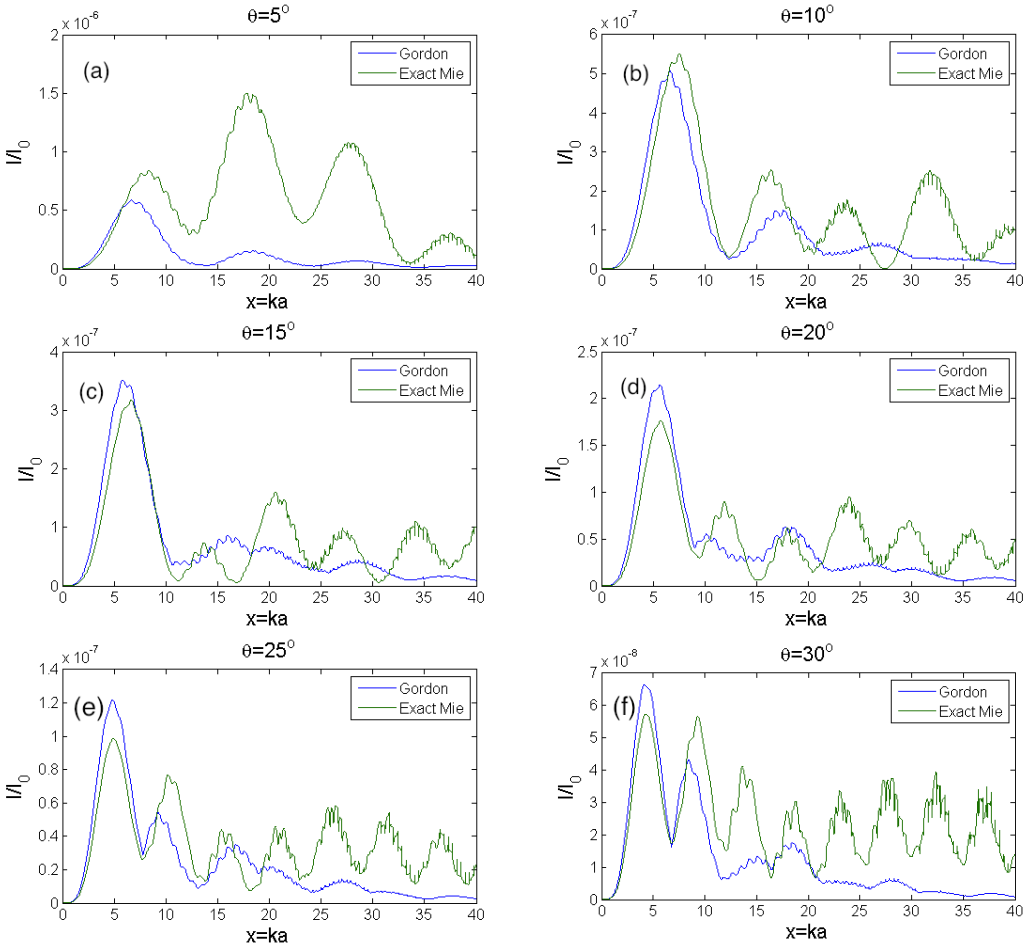

Figure 3.6: Plots of Gordon's approximation versus the exact Mie solution at different scattering angle θ. The y-axis shows the relative intensity $I(\theta)/I_0$ at the given solid angle: **a**: $\theta = 5^o$, **b**: $\theta = 10^o$, **c**: $\theta = 15^o$, **d**: $\theta = 20^o$, **e**: $\theta = 25^o$. **f**: $\theta = 30^o$

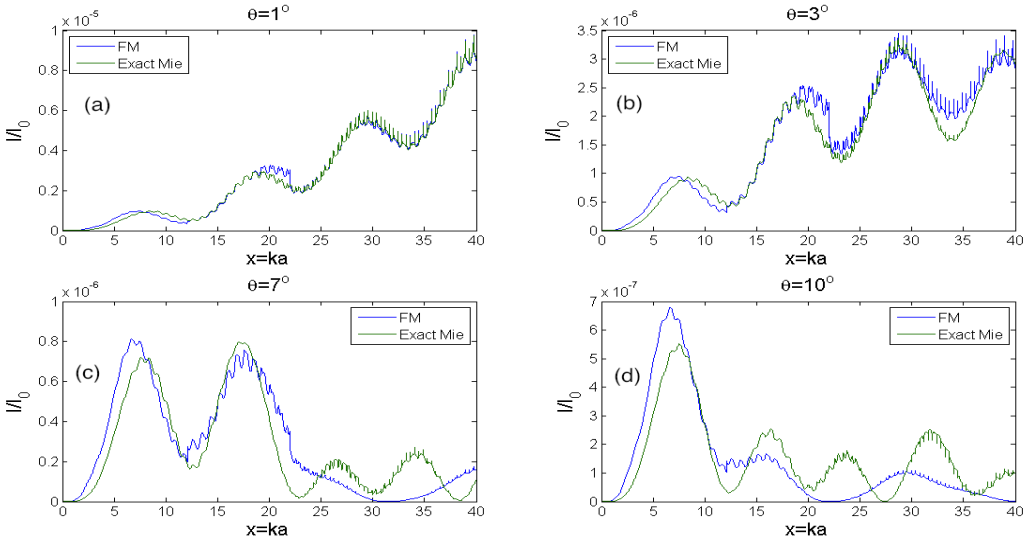

Figure 3.7: Plots of Fymat and Mease's approximation versus the exact Mie solution at different scattering angle θ. The y-axis shows the relative intensity $I(\theta)/I_0$ at the given solid angle: **a**: $\theta = 1^o$, **b**: $\theta = 3^o$, **c**: $\theta = 7^o$, **d**: $\theta = 10^o$.

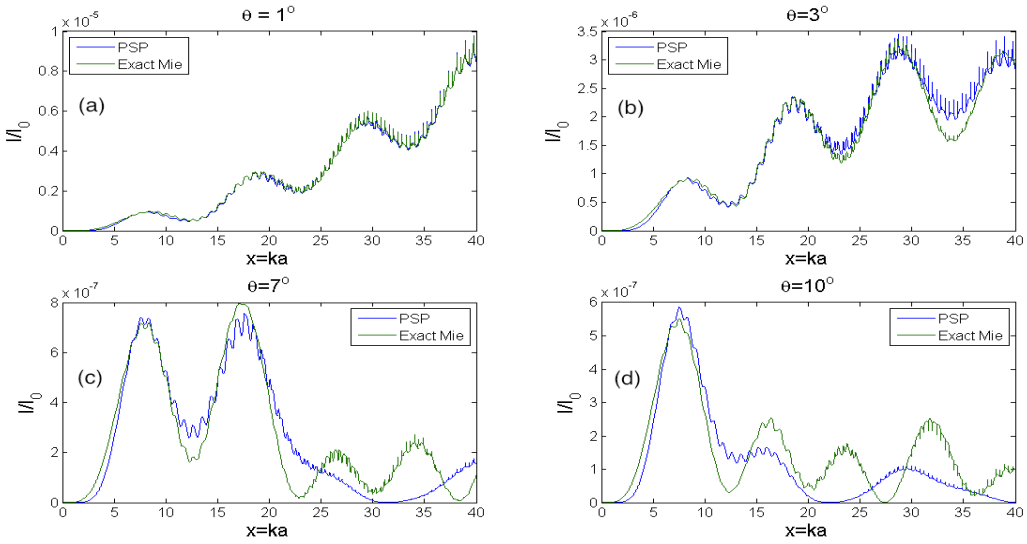

Figure 3.8: Plots of Penndorf, Shifrin and Punina's approximation versus the exact Mie solution at different scattering angle θ. The y-axis shows the relative intensity $I(\theta)/I_0$ at the given solid angle: **a**: $\theta = 1^o$, **b**: $\theta = 3^o$, **c**: $\theta = 7^o$, **d**: $\theta = 10^o$

3.4.1 Integrating the scattering efficiency

The scattering efficiency curve is calculated from the the relative intensity formula acquired from the approximation formulas made by Fymat & Mease and by Gordon. The relative intensity at a point with the distance r from the sphere has the form [11]:

$$\frac{I(\theta)}{I_0} = \frac{i_1(\theta) + i_2(\theta)}{2k^2r^2} \tag{3.26}$$

Where I_0 is the intensity of the incident light, k is the wavenumber and i_1 and i_2 is the intensity component perpendicular and parallel to the scattering plane respectively. To get the relative intensity independent of the distance from the sphere, i.e. the radial intensity, the unit of steradians is introduced: $1sr = r^2$. The relative intensity in eq. 3.26 is now:

$$\frac{I(\theta)}{I_0} = \frac{i_1(\theta) + i_2(\theta)}{2k^2} \tag{3.27}$$

with the unit of solid angles $[sr^{-1}]$. The relative intensity of equation 3.27 is the intensity of an area r^2 divided by the incident intensity.

The scattering efficiency Q_{NA} is given in equation 3.2, the integrand $(i_1 + i_2)$ can be replaced by $2k^2\ I(\theta)/I_0$, as can be seen from equation 3.27. Thus the efficiency for the numerical aperture can be expressed as:

$$Q_{\mathrm{NA}} = \frac{2}{a^2} \int_0^{\theta_{\mathrm{NA}}} \frac{I(\theta)}{I_0} \sin\theta d\theta \tag{3.28}$$

The factor a^{-2} in equation 3.28 might seem troublesome, remembering the scale invariance statement in section 2.1. This problem is resolved in the PSP/FM approximation by the equation giving the Fraunhofer approximation (eq. 3.19, which contains the factor $x^2/k^2 = a^2$ going against a^{-2} in formula for Q_{NA} (eq. 3.28).

The same problem is resolved in the Gordon approximation by the k^{-2} dependence of the incident intensity (eq. 3.25), which is multiplied with the a^{-2} in equation 3.28, making Q_{NA} dependent only on the size parameter x.

Four approaches are used to estimate Q_{NA}:

1. Only the PSP approximation is used to estimate Q_{NA}. The intensities are calculated by the PSP approximation (eq. 3.20).
2. Only the FM approximation is used to estimate Q_{NA}. The intensities are calculated by the FM approximation (eq. 3.23).
3. The PSP approximation (eq. 3.20) is used to calculate the intensities at low angles, $\theta \in [0^o, 10^o]$. For $\theta \in [10^o, \theta_{\mathrm{NA}}]$ the Gordon approximation (eq. 3.24) is used to calculate the intensities.

4. The FM approximation (eq. 3.23) is used to calculate the intensities at low angles, $\theta \in [0^o, 10^o]$. For $\theta \in [10^o, \theta_{\mathrm{NA}}]$ the Gordon approximation (eq. 3.24) is used to calculate the intensities.

The reason for combining the approximations, PSP/FM and Gordon, is that the PSP/FM approximations is more accurate at small angle intensities, while the Gordon approximation is more accurate at higher angles. The angle $\theta = 10^o$ for switching between approximations is chosen by visual inspection of $I(\theta)/I_0$. Figures 3.7 and 3.6 show that the two approximations have about the same accuracy at an angle of 10^o, making this angle a reasonable choice.

An integration using only Gordon's approach is not included since this approximation, as illustrated in figure 3.6 does not give a good result at small angles. Small angles have higher scattering intensities than the larger angles, thus the Gordon approximation alone is bound to be worse than the PSP and FM approximation alone for integrations including the angles in the near forward direction.

The modulating function $\gamma(x_g)$ is chosen in a different way as in the article by Gordon. A dependency on θ as well as x_g was introduced. This is done to improve the result for a larger range of angles. The γ used in this thesis is an ad hoc version of the function, that has been adapted to the best fit for the purpose described in this section. This γ should not be put too much attention to, since other γ's could serve this purpose just as well. The γ used in this integration can be found in the MATLAB function *Gordon.m* in appendix B.2.

The MATLAB program used to integrate Q_{NA} is found in appendix B.1. This program use the MATLAB functions found in appendix B.2. The other functions used are Mätzlers MATLAB functions, and can be found in the reference [19].

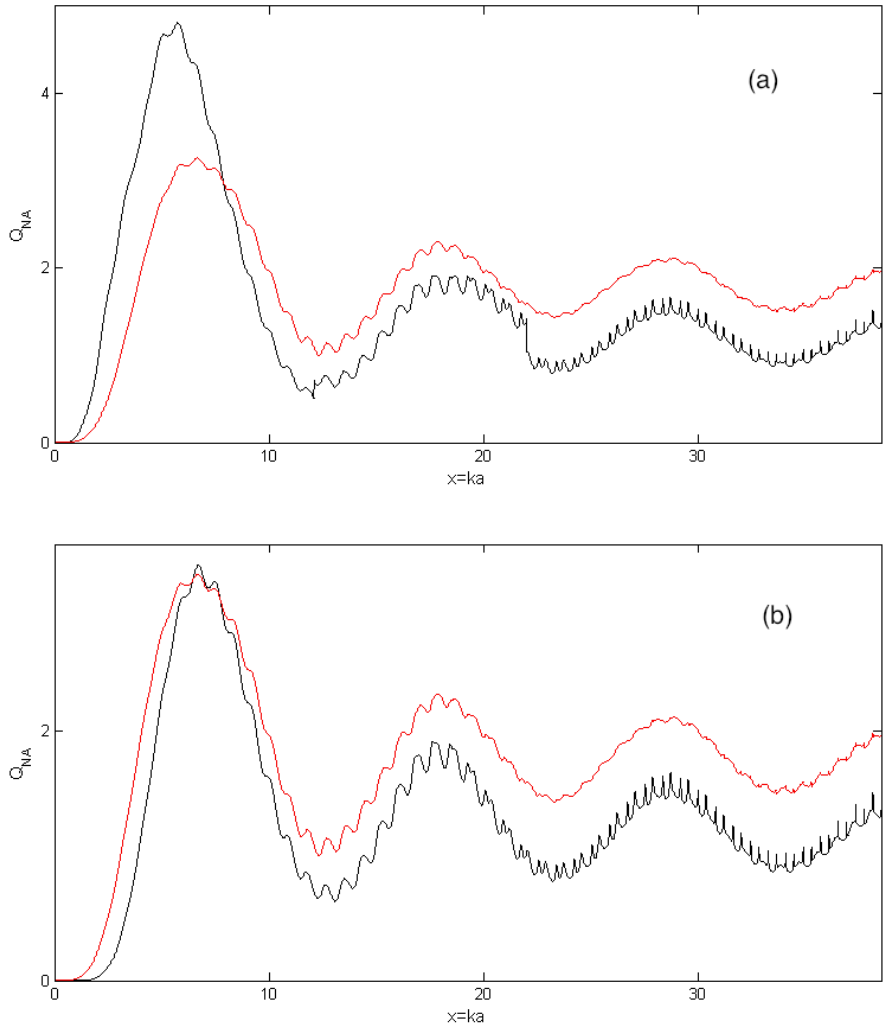

Figure 3.9: **a**: The black line shows the Q_{NA} calculated by the Fymat & Mease (FM) approximation integrated over interval $\theta \in [1^o, 35^o]$ (approach 2), while the red line is the exact Q_{NA} in the same interval. The refractive index $m = 1.3$. **b**: The black line shows the Q_{NA} calculated by the Penndorf, Shifrin & Punina (PSP) approximation integrated over interval $\theta \in [1^o, 35^o]$ (approach 1), while the red line is the exact Q_{NA} in the same interval. The refractive index $m = 1.3$.

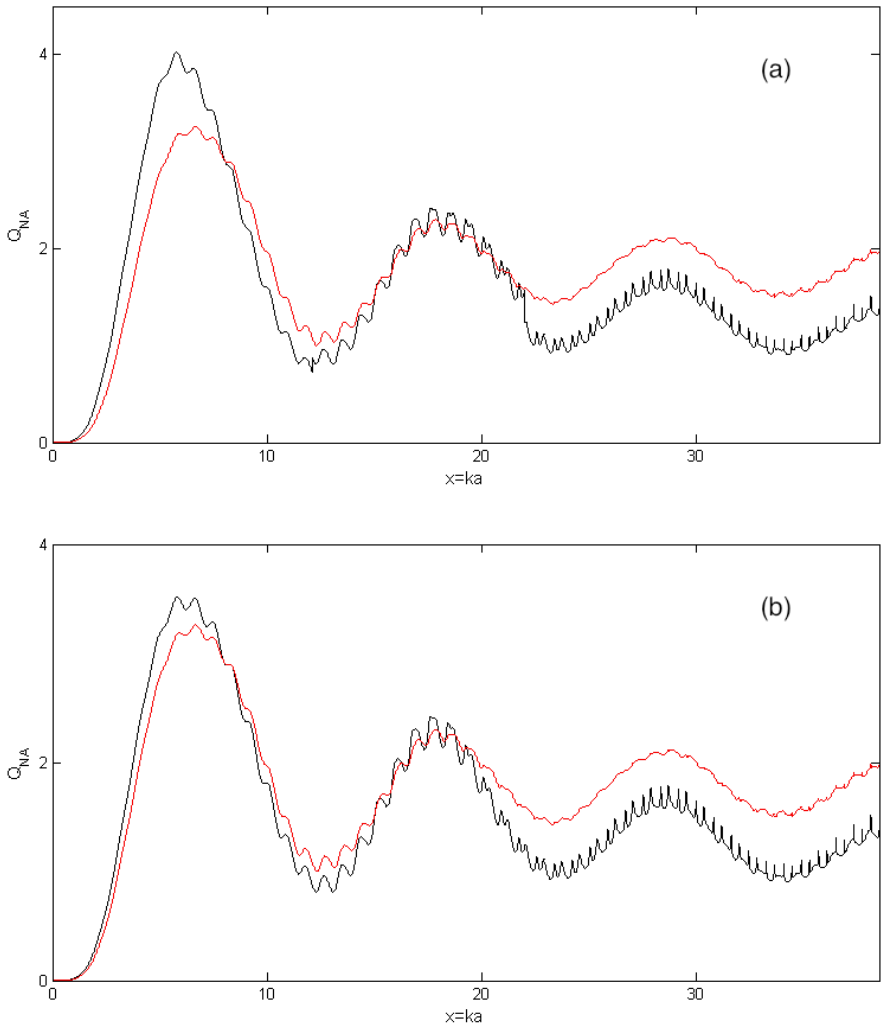

Figure 3.10: **a**: The black line shows the Q_{NA} calculated by the Fymat and Mease (FM) approximation combined with Gordon's approximation integrated over interval $\theta \in [1^o, 35^o]$ (approach 4), while the red line is the exact Q_{NA} in the same interval. **b**: The black line shows the Q_{NA} calculated by the Penndorf, Shifrin and Punina (PSP) approximation combined with Gordon's approximation integrated over interval $\theta \in [1^o, 35^o]$ (approach 3), while the red line is exact Q_{NA} in the same interval.

In figure 3.9 the approximation is done by integrating the PSP approximation (fig. 3.9 **b**) or FM approximation (fig. 3.9 **a**) over the interval of solid angles $\theta \in [1^o, 35^o]$, corresponding to approach 1 and 2 in the list above. In figure 3.10 the integration is done by integrating the PSP approximation (fig. 3.10 **b**) or the FM approximation (fig. 3.10 **a**) for $\theta \in [1^o, 10^o]$, and the Gordon approximation for $\theta \in [11^o, 35^o]$, corresponding to approach 3 and 4 respectively. The approximations have in general the same shape as the exact solution with different degree of accuracy, but some essential differences are worth noticing:

1. The high frequent oscillations, called wiggles (smooth and wavelike) and ripples (sharp and narrow), seem to have the same phase in the approximation and the exact solution, but the wiggles and ripples in the approximation is more intense than in the real solution. This is most likely because the PSP and FM approximation is modeled around the square of the forward extinction curve (eq. 3.20). The Fraunhofer diffraction formula (eq. 3.19) used to estimate the the scattered intensity at different angles does not contain information on how the wiggles vary in size with the angles. In figure 3.7 we see that the wiggles are overestimated in amplitude, especially at low angles.

2. In approach 2 and 4 (figure 3.9 a and figure 3.10 a) the approximations exhibits some jumps that are caused by the discontinuous functions in eq. 3.22. In approach 1 and 3 (figure 3.9 b and figure 3.10 b), the PSP approximation is used instead of the FM approximation, leaving out the extension done by Fymat and Mease (eqs. 3.21 and 3.22). As seen in these plots, the discontinuities are gone, and the approximation are equally or more accurate than the approaches where the FM approximation is used.

3.4.2 Comparison of errors in the approximations

To compare the approximation approaches 1-4 in one plot, the relative error from the exact solution is calculated. The area of the plots focuses on the region between $x = 0$ and $x = 15$, which is the region with the most interesting differences. At values of x higher than 15 the differences between the different approaches are small and the are hard to make out because of the ripples obstructing the graphs. Figure 3.11 shows the relative error between the approximations and the exact Mie solution, ε_{rel}, per value of x is calculated by the formula:

$$\varepsilon_{rel}(x) = \frac{Q_{\mathrm{NA},Mie}(x) - Q_{\mathrm{NA},Approx}(x)}{Q_{\mathrm{NA},Mie}(x)} \tag{3.29}$$

Where $Q_{\mathrm{NA},Mie}$ is the exact efficiency factor for the numerical aperture, and $Q_{\mathrm{NA},Approx}$ is the efficiency factor of the numerical aperture calculated using an approximation.

Figure 3.11 shows the relative error at different indexes of refraction. The plots show a relative error ε_{rel} which holds relatively steady at different refractive indices. Also a decrease in error with increasing refractive index is sometimes observed.

The plots in figure 3.11 show that the integrations done combining the PSP approximation and FM approximation combined with the Gordon approximation (approach 3 and 4) performs best. This can easily be seen in the plots showing ε_{rel} for refractive indices $m = 1.3$ and $m = 1.4$, where the relative errors in approach 3 and 4 lies closer to the zero-line (marked as 'Exact Mie' in the plots) than the others. The FM approximation alone (approach 2) preforms rather poorly for $m = 1.3$; e.g. it drops below -4 at $x \sim 2$, indicating that the approximated Q_{NA} is four times higher than exact Q_{NA}. Figure 3.9 shows that the absolute difference is also large for approach 2. In figure 3.11 **c** and **d** showing ε_{rel} for $m = 1.5$ and 1.6 approaches 1 and 2 (not including the Gordon approximation) performs better than for $m = 1.3$ and $m = 1.4$, while approaches 3 and 4 (including the Gordon approximation) performs at about the same level of validity. Of approaches using the Gordon approximation (approach 3 and 4), the one using the PSP approximation (approach 3) seems to perform best.

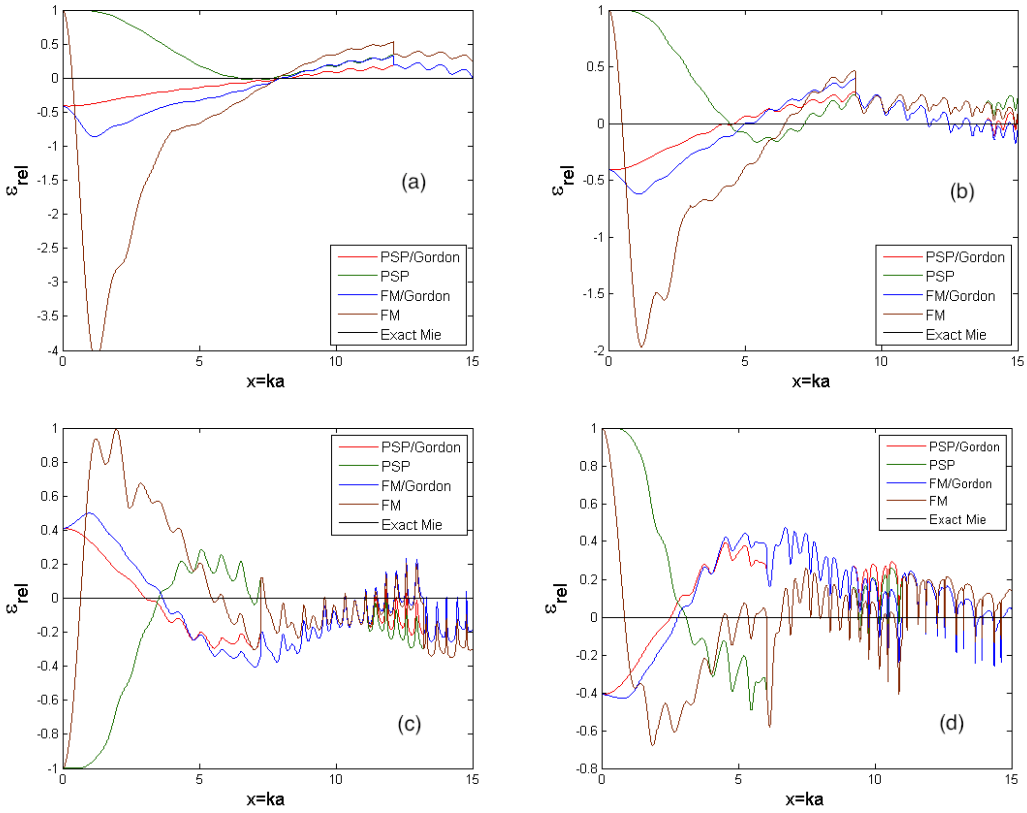

Figure 3.11: The relative difference from the exact solution for all four approaches for approximating Q_{NA} with a $\theta_{\mathrm{NA}} = 35$. Each plot shows ε_{rel} calculated with different refractive indices: **a**: $m = 1.3$, **b**: $m = 1.4$, **c**: $m = 1.5$ **d**: $m = 1.6$.

3.5 Approximations modulated from approximate forward extinction

In the following the best performing approach from section 3.4.1, which is the approach combining the Penndorf, Shifrin and Punina approximation ($\theta \in [1^o, 10^o]$) and the Gordon approximation ($\theta \in [11^o, \theta_{\mathrm{NA}}]$), is modified to give a pure approximation. This means that the forward amplitude I_0 and the forward extinction efficiency Q_{ext} used to construct the approximations in the non-forward direction, is achieved from an approximation instead of the exact Mie solution. The forward approximation used is the Anomalous Diffraction Approximation (ADA), described in section 3.2.1.

The extinction efficiency Q_{ext} is calculated using equation 3.10 and the intensity $I(0)$ in the forward direction is calculated by equation 3.25. The amplitude functions in the forward direction $S(0)$ is given by the equation 3.8. An assumption for the anomalous diffraction approximation is that $m - 1 \ll 1$, therefore this approximation method for Q_{NA} is expected also to work best in this range.

The efficiency associated with the numerical aperture Q_{NA} modeled after ADA is shown in figure 3.12. The plots are made using different refractive indices. As expected the approximation works best for low values of m. The ripples shown in the real solution are not present in the approximation since they are not explained by the anomalous diffraction theory.

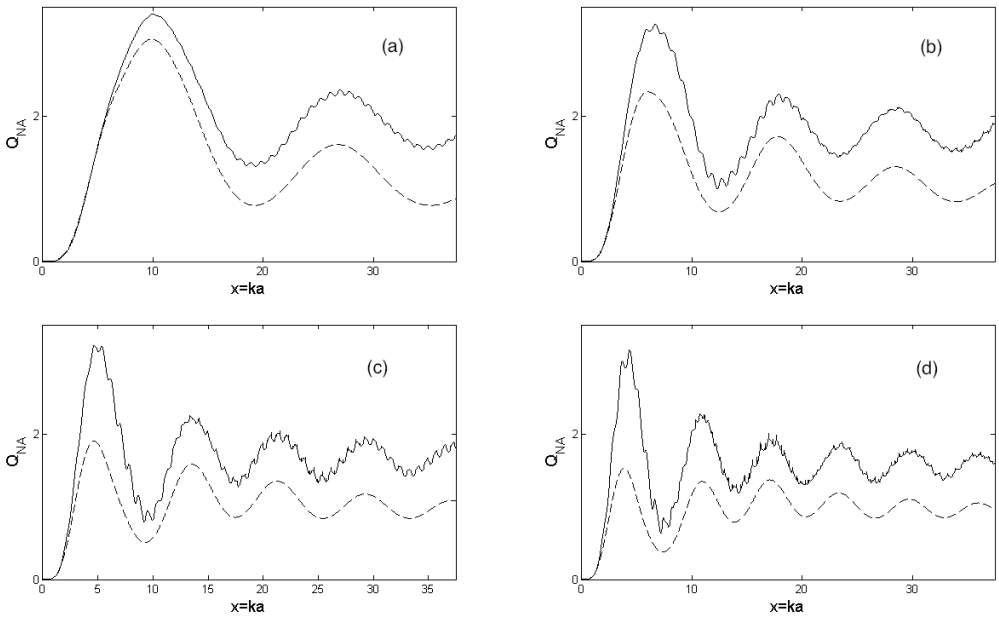

Figure 3.12: The exact solution and the anomalous diffraction approximation (ADA) integrated a region of solid angels $\theta \in [0^o, 35^o]$ to give Q_{NA} for different values of refractive index m. The exact solution is shown as a solid line, and the anomalous diffraction is shown as a striped line. **a**: $m = 1.2$, **b**: $m = 1.3$, **c**: $m = 1.4$, **d**: $m = 1.5$.

3.6 Estimating Mie-scattering in infrared microspectroscopy of pollen

To test the approximation of the Mie solution in biological applications, real spectra of spherically shaped biological particles are obtained. These were made by synchrotron based FTIR-spectroscopic analysis of a single pollen grain from the species *Juniperus Excelsa*. The measurements of the spectra were recorded at the SOLEIL synchrotron facility. The image in figure 3.13 shows the analyzed pollen grain and the infrared beam illuminating the particle. The scale is shown at the axes of the image, making it possible to visually estimate the size of the particle, which in this case can be estimated to about 22 μm. The only unknown parameter of the sample is the refractive index, which is reasonable to assume lies within the range 1.3 to 1.5 [24,25].

The microscope used is a Nicolet Continuum XL with 15× objective, giving a numerical aperture (NA) = 0.58. From equation 2.45 you find that this corresponds to

a spherical cap with angle $\theta_{\mathrm{NA}} \simeq 35.5^o$. This means that the light scattered with an angle smaller than θ_{NA} will not be a part of the scattering. The efficiency of the numerical aperture (eq. 3.2) can be written as:

$$Q_{\mathrm{NA}} = \int_0^{35.5^o} Q_{sca}(\theta) d\theta \tag{3.30}$$

The equation stating that $Q_{ext} = Q_{sca} + Q_{abs}$ (eq. 2.23) can be used to estimate Q_{abs} if Q_{ext} is replaced with $Q_{ext,\mathrm{NA}}$, and Q_{sca} is replaced with $Q_{sca,\mathrm{NA}}$:

$$Q_{abs} = Q_{ext,\mathrm{NA}} - Q_{sca,\mathrm{NA}} \tag{3.31}$$

The term $Q_{ext,\mathrm{NA}}$ in equation 3.31 will be the extinction in the measured data. By subtracting the term $Q_{sca,\mathrm{NA}}$, which is the scattered light not collected by the focusing optics, the absorption efficiency Q_{abs} will appear. The IR-spectrum in figure 3.14 is the absorbance $A = -\log_{10}(T)$ (eq. 2.43) of the pollen grain. The estimated scattering contribution is not equivalent with the absorbance [2], but is often interpreted as the scattering contribution to the absorbance spectrum [16]. This is done also in this thesis, although it is a rough estimation.

In figure 3.14, one of the absorbance spectra from the spectroscopic analysis of the pollen is shown together with the estimated $Q_{sca,\mathrm{NA}}$. The efficiency of the numerical aperture Q_{NA} is estimated by the 3. approach in section 3.4.1, combining the PSP and Gordon approximation. The spectrum is obtained from the pollen grain illuminated in the image in fig 3.13. The radius is $a = 11\ \mu m$ and integration is done for the range of angles $\theta \in [1^o, 35^o]$. The refractive index was chosen to be 1.31 since it visually yielded the best fit for the spectrum.

The parameters for the estimated Mie scattering are chosen with a high degree of uncertainty. In addition the pollen grain is no a perfect homogeneous sphere. Thus the corrected spectrum in fig. 3.14 **b** is not nessicarily the spectrum showing only the absorption bands, but merely illustrate that the scattering somewhat coincides with the part of the uncorrected absorbance spectrum in figure 3.14 **a** expected to be the scattering contribution.

[2] The relation between transmission, absorption and the extinction efficiency is presented in section 2.5

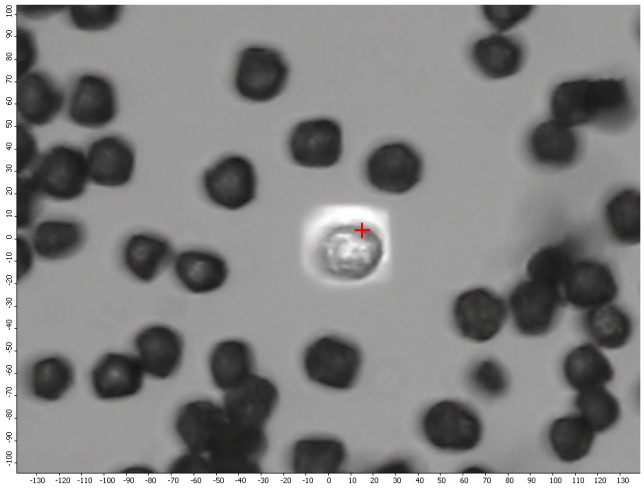

Figure 3.13: Microscopic image of the analyzed pollen grain from the species *Juniperus Excelsa*. The beam is 20×20 μm, and the diameter of the pollen grain is about $22\mu m$ estimated by comparison with the axes on the edge of the image.

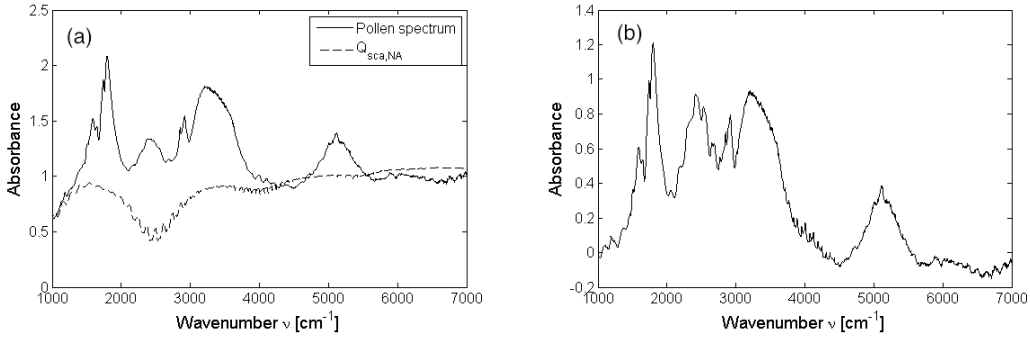

Figure 3.14: **a**: The absorbance spectrum from the analysis of the pollen grain with contributions from Mie-scattering, and the estimated Mie-scattering contribution $Q_{sca,\mathrm{NA}}$. **b**: The absorbance spectrum with the estimated scattering contribution subtracted. The wavenumber on both plots are $\tilde{\nu} = 1/\lambda$ $[cm^{-1}]$

4 The ripple structure

The exact Mie extinction show a rapidly fluctuating structure that breaks with the smooth wavelike underlying structure. The sharp narrow structure is called ripples, while the broader and smoother structure is called wiggles. In figure 4.1 the wiggles and ripples are shown more explicitly. Bohren and Huffman [18] presents a classical electromagnetic solution in terms of the normal modes, or resonant modes, of the electric field. This will be the topic of the next section (4.1). To get more insight in the origin of the wiggles and ripples in terms of scattering, a semiclassical approach where the scattering of electromagnetic waves is viewed as a quantum mechanical problem is discussed. This way we can speak of rays of light as particle paths and look at their individual contribution to the scattering [26]. In the ray picture, resonant modes are equivalent to orbits (sec. 4.2) of the individual rays. Many of them have a simple geometrical interpretation. In section 4.3 the ripples in the extinction efficiency curve are Fourier transformed and analyzed in light of the ray picture.

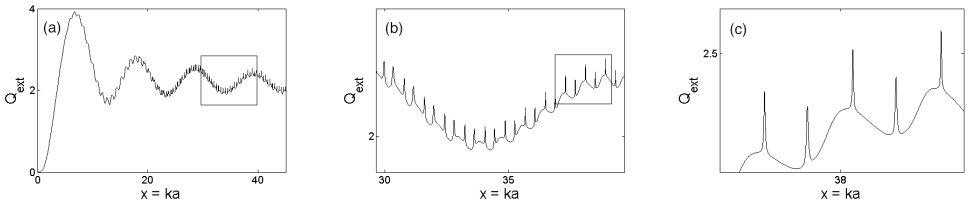

Figure 4.1: **a**: The extinction efficiency curve of the exact solution. **b**: The extinction efficiency curve zoomed in on the box in **a**. **c**: The extinction efficiency curve zoomed in on the box in **b**; the ripples are shown as sharp, narrow peaks and the wiggles are the smoother and wider fluctuations.

4.1 Electromagnetic normal modes[1]

The solution to the vector wave equation for a sphere is the basis for Mie's theory for scattering by a sphere. The solutions that satisfy the scalar wave equation in spherical coordinates A.20 are presented as an odd and an even wave function [18]:

$$\psi_{emn} = \cos m\phi P_n^m(\cos\theta) z_n(kr) \tag{4.1}$$

$$\psi_{omn} = \sin m\phi P_n^m(\cos\theta) z_n(kr) \tag{4.2}$$

Where $P_n^m(\cos\theta)$ is the associated Legendre function and $z_n(kr)$ is the first or second kind of the spherical Bessel functions. Any function that satisfies the scalar wave equation can be written as an infinite series of the equations 4.1 and 4.2. The vector spherical harmonics $\mathbf{M}_{emn}$, $\mathbf{M}_{omn}$, $\mathbf{N}_{emn}$ and $\mathbf{N}_{omn}$ are generated by ψ_{emn} and ψ_{omn}, and are given in the appendix (A.4.1).

The incident light described as a plane wave is usually written as $\mathbf{E}_i = E_0 e^{ikr}\hat{k}$. The plane wave can also be written in vector spherical harmonics, with the electrical field:

$$\mathbf{E}_i = E_0 \sum_{n=1}^{\infty} i^n \frac{2n+1}{n(n+1)} (\mathbf{M}_{oln}^{(1)} - i\mathbf{N}_{eln}^{(1)}) \tag{4.3}$$

and magnetic field:

$$\mathbf{H}_i = \frac{-k}{\omega\mu} E_0 \sum_{n=1}^{\infty} i^n \frac{2n+1}{n(n+1)} (\mathbf{M}_{eln}^{(1)} + i\mathbf{N}_{oln}^{(1)}) \tag{4.4}$$

where μ is the magnetic permittivity and the superscript (1) indicates the first kind of the spherical Bessel functions. The condition at the boundary between the sphere and the surroundings is stated to be [18]:

$$(\mathbf{E}_i + \mathbf{E}_s - \mathbf{E}_l) \times \hat{\mathbf{n}}_r = (\mathbf{H}_i + \mathbf{H}_s - \mathbf{H}_l) \times \hat{\mathbf{n}}_r = 0 \tag{4.5}$$

The field inside the sphere $\mathbf{E}_l$ can be expressed the same way as the incident field, but with scaling coefficient c_n applied to the odd versions of $\mathbf{M}^{(1)}$ and $\mathbf{N}^{(1)}$, and d_n applied to the even ones. The scattered field E_s has has the coefficients a_n for the even terms of $\mathbf{M}^{(3)}$ and $\mathbf{N}^{(3)}$, and b_n for the odd ones:

$$\mathbf{E}_s = \sum_{n=1}^{\infty} E_n (i a_n \mathbf{N}_{eln}^{(3)} - b_n \mathbf{M}_{oln}^{(3)}) \tag{4.6}$$

[1]This section about the incident, scattered and internal electromagnetic fields represented in spherical harmonics is based on the results of the derivation in Bohren and Huffman [18], this also applies for the discussion of the normal modes and their relevance to the ripple structure in Mie solutions to scattered light.

where $E_n = i^n E_o(2n+1)/(n(n+1))$. The superscript (3) indicates that the third kind of the spherical Bessel functions is used (the first kind of the spherical Hänkel functions).

The vector spherical harmonics $\mathbf{M_n}$ and $\mathbf{M_n}$ each represent a normal mode of the spherical particle. The scattered field is a superposition of normal modes, but under certain conditions a single normal mode will be exited. For each n there are two types of modes: transverse magnetic modes (E-wave), for which there are no radial magnetic component and transverse electric modes (H-wave), for which there are no radial electric component[2]. The normal mode for a particular n will appear in the scattered field when the denominator in a_n (eq. 2.32) or b_n (eq. 2.33) is very small. The appearance of these normal modes depends on x, which is dependent on the frequency of the incident light. Since Q_{ext} (and also the amplitude functions) is a sum over all a_n and b_n, the resonant normal modes give a contribution to Q_{ext} at the values of x where the normal modes appear. The top of each ripple then appears at the resonance frequency for a normal mode.

4.2 Semiclassical scattering

4.2.1 Ray picture of scattering

In the problem of scattering by a sphere, the resonances in the Mie coefficients a_n and b_n is what makes the ripples appear in the extinction curve. Each of the resonances can be viewed upon as one partial wave in the total sum of the S-functions (eqs. 2.28 and 2.29) contributing a lot more to the scattering than the others. The physical interpretation of this is not very clear, and a more intuitive way of understanding the resonances would be of help to analyze the ripple structure.

A way to interpret the resonances is to view the individual partial waves of the scattering functions as rays which undergo multiple reflections inside the sphere. The rays hit the walls of the sphere beyond the critical angle indicating total reflection. At the resonance the ray makes an integral number of reflections inside the sphere and returns to its starting point in phase. [27]

Orbits reachable by geometrical optics can account for the broader resonances, i.e. the wiggles, but the resonances that shows the sharp, narrow ripples in the highest detailed plot in figure 4.1, does not originate from orbits reachable from the outside by classical means. The ripples are associated with rays undergoing total internal

[2]The electric field of the oscillating electric dipole corresponds to the normal mode a_1, which is the first E-wave mode

reflection, and cannot be reached from the outside by simple refraction. Diffraction must occur to redirect the ray to enter the sphere at angles not allowed by refraction and reflection. The rays undergoing total internal reflection gives an increase of energy density near the surface of the sphere, since the ray may undergo a large number of orbits with a small amount of leakage to the outside. Orbits that reflects a large number of times inside the sphere beyond the limit of total reflection, are sometimes called "whispering gallery" modes. [27, 28]

The ray picture of scattering of light can be useful since the trajectories of the rays are analogous with the trajectories of particles described by quantum mechanics.

The next section 4.2.2 will give an example of a quantum mechanical approach to a classical problem; the scattering of electromagnetic waves in one dimension, and how this gives a picture of rays instead of a continuous wave. This gives a simple connection between the orbits and the ripple structure. The section 4.2.3 will in more detail go through the orbits and ray dynamics in terms of semiclassical scattering.

4.2.2 Scattering in one dimension - equivalency between classical and quantum mechanics

In classical electrodynamics the problem of a traveling electromagnetic wave incident to the surface of a slab represents a one-dimensional scattering problem. A part of the wave is reflected at the boundary between the ambient medium and the slab, and the rest is transmitted across the boundary. A second part of the wave is reflected at the second boundary between the slab and the ambient medium, while the rest is transmitted into the ambient medium again. The electric field of the wave impinging the slab described by $\tilde{E}(x,t) = \tilde{E}(x)e^{i\omega t}$ satisfies the Helmholtz equation [16]:

$$\left[\frac{d^2}{dx^2} + \varepsilon_r k_0^2\right] \tilde{E}(x) = 0 \tag{4.7}$$

where ε_r is the relative dielectric constant and k_0 is the wavenumber . The electric field amplitude in regions I, II and III in figure 4.2 can be found by Imposing the boundary conditions that the electric field is continuous and smooth across the boundaries, giving the amplitudes of the reflected and the amplitude of the transmitted field. The transmission amplitude obtained by the solution to this problem is [16]:

$$t = \frac{2ime^{-ika}}{(1+m^2)\sin(mka) + (2im\cos(mka)} \tag{4.8}$$

where k is the wavenumber, m is the refractive index and a is the thickness of the slab.

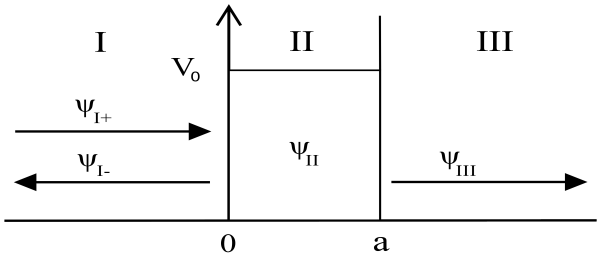

Figure 4.2: The setup of quantum mechanical case of a particle that hits potential barrier. The wave functions in region I and III describes a free particle ($V(x) = 0$) with the constraint of a continuous and smooth function at the boundaries of region II, where the potential is $V(x) = V_0$.

The setup of the Helmholtz equation (eq. 4.7) is an equivalent setup to the quantum mechanical case of particles impinging a square potential (figure 4.2). In the following the quantum mechanical case is solved. The stationary Schrödinger equation with a constant potential V_0 in the region $0 > x > a$ is given as:

$$\left[\frac{-\hbar^2}{2m}\frac{d^2}{dx^2} + V(x)\right]\psi(x) = E\psi(x), \quad V(x) = \begin{cases} V_0, & \text{for } 0 \leq x \leq a \\ 0, & \text{otherwise} \end{cases} \tag{4.9}$$

Where $V(x)$ is the potential function, $\hbar$ is Planck's constant and m is the mass of the particle. The solution to the Schrödinger equation for each of the areas I, II and III in figure 4.2 is [29]:

$$\psi_{\mathrm{I}}(x) = e^{ik_1 x} + re^{-ik_1 x}, \text{ for } x \leq 0 \tag{4.10}$$

$$\psi_{\mathrm{II}}(x) = Ae^{ik_2 x} + Be^{-ik_2 x}, \text{ for } 0 \leq x \leq a \tag{4.11}$$

$$\psi_{\mathrm{III}}(x) = te^{ik_1 x}, \text{ for } a \leq x \tag{4.12}$$

Where r is the reflection amplitude and t is the transmission amplitude. The amplitudes are found by imposing the same boundary conditions as is the classical case: the wave function needs to be continuous and smooth (continuous derivative) at the boundaries. The constants $k_1 = \sqrt{2mE/\hbar^2}$ and $k_2 = \sqrt{2m(E - V_o)/\hbar^2}$ for respectively outside and inside the potential barrier. The boundary conditions states that $\psi_{\mathrm{I}}(0) = \psi_{\mathrm{II}}(0)$, $\psi_{\mathrm{II}}(a) = \psi_{\mathrm{III}}(a)$, $\psi'_{\mathrm{I}}(0) = \psi'_{\mathrm{II}}(0)$ and $\psi'_{\mathrm{II}}(a) = \psi'_{\mathrm{III}}(a)$. This gives the transmission amplitude:

$$t = \frac{2k_1 k_2 e^{-ika}}{2k_1 k_2 \cos(k_2 a) - i(k_1^2 + k_2^2)\sin(k_2 a)} \tag{4.13}$$

If the constants k_1 and k_2 translates to the wave numbers, then this expression is the same as in the classical solution in 4.8 with a little rearranging, and by setting $k_1 = k$,

which is the wavenumber in the ambient medium and $k_2 = mk$ the wavenumber inside the slab, where m is the refractive index of the medium in the slab and k is the wavenumber of the electromagnetic wave outside the slab.

In the further discussion, a formula for the transmissivity, or transmission probability can be given. The transmissivity is $T = |t|^2$, assuming no absorption [29]. The expression for T is:

$$T = |t|^2 = \frac{1}{1 + \frac{1}{4}\left(\frac{1}{m} - m\right)^2 \sin^2(mka)} \tag{4.14}$$

From eq. 4.14 we can see that when $\sin mka$ is zero, the transmissivity is 1. This happens when $mka = n\pi$, where $n = 1, 2, 3, ...$ These states are the bound quantum mechanical states. They also correspond to the states when the electric field oscillates one or one half wavelength between the boundaries of the slab. These can be translated into the normal modes of the electric field in the slab. A physical interpretation can be that the electromagnetic wave reflected at the inner boundary (between regions II and III in fig. 4.2) will interfere destructively with the wave reflected at the outer boundary (between regions I and II in fig. 4.2), annihilating the reflected wave completely. Thus by the conservation of energy principle, the transmitted wave must be as energetic as the incident wave. The number n can be interpreted as the number of bounces the electromagnetic wave makes at the internal boundary. When the electromagnetic wave bounces more than once off the boundary between regions I and II, n will be larger than one. By the same argumentation, the reflectivity is the largest when $mka = \frac{n\pi}{2}$. In between these extremal points there will be more or less interference between the reflected waves, making up the wiggles seen in infrared spectroscopy of a slab (often referred to as fringes).

The correspondence between the classical and the quantum mechanical case of one dimensional scattering of a finite potential barrier illustrates a case of semiclassical scattering; the scattering of particles as an analogy to the scattering of electromagnetic waves.

4.2.3 Scattering by a sphere - ray dynamics

In this section an attempt will be made to discuss scattering by a sphere in terms of ray dynamics and introduce semiclassical scattering by a sphere. We start by introducing the localization principle, from which van de Hulst connected number of terms n in the Mie scattering amplitudes (eqs. 2.28 and 2.29) to the quantum mechanical angular momentum number, l.

The localization principle [11] states that a term in the Mie solution of the order n corresponds to a ray passing through the sphere at a distance $d = (n + \frac{1}{2})\lambda/2\pi$ from

the origin, where λ is the wavelength of the light. The distance $n + 1/2 = x$, where x is the size parameter, is exactly the radius of the sphere, meaning that terms with $n + 1/2 < x$ correspond to rays hitting the sphere, while terms with $n + 1/2 > x$ correspond to rays passing the sphere. The contribution to the Mie solution from the rays passing the sphere goes to zero with increasing n.

The connection with quantum mechanics is by van de Hulst introduced by the analogy of an electron colliding with a central potential. The solution has the form of a series with integer values of angular momentum l, and the average distance of the electron from the centre is $d = (l + \frac{1}{2})\lambda/2\pi$, where λ is the de Broglie wavelength of the electron. [11]

The orbits obtainable by refraction, called the open channels, correspond to the rays with a distance from the origin of the sphere $d < x$, which in semiclassical scattering is obtained by having an angular momentum $l < l_{max}$, where l_{max} is the angular momentum giving $l + \frac{1}{2} = x$. The rays having $l > l_{max}$ is called the closed channels, and have by the localization principle, a distance from the origin larger than the radius of the sphere. In the ray picture these rays pass the origin outside the sphere, but may in semiclassical scattering enter and the sphere through tunneling, and turn into the high energy orbits mentioned in the introduction to this section 4.2. [11,13]

By looking at each partial waves of the amplitude functions in the forward direction (eq. 2.28 and 2.29) as rays, each ray S_l is the l-th term in the sum. The subscript l denotes angular momentum of the semiclassical ray. By the localization principle, each orbit will originate from one partial wave. The ray represented by the term S_0 will have zero angular momentum, and therefore go through the centre of the sphere. This will be similar to scattering by a slab in section 4.2.2. By analyzing only the S_0 component of the amplitude function, only the diameter orbit is obtainable, and the ripples should be like the "fringes" of the 1-D scattering problem. [13]

4.3 Analysis of the ripples in Q_{ext}

To analyze the ripples caused by the open channels (obtainable by refraction) orbits in Q_{ext}, one can use Snell's law of refraction to determine the change of angel of the incident light. The light will, at a certain displacement from axis going through the origin of the sphere, refract in such a way that the ray will bounce two times inside the sphere and exit in the direction of the incident light. This is called a triangular orbit and is shown in figure 4.3 **b** and **d**. Rays which go through the centre of the sphere will have no change of angle. These orbits correspond to the one dimensional case described in section 4.2.2, and are shown in figure 4.3 **a** and **c**. For the triangular orbit (fig. 4.3 **b**), the angle of refraction α related to the incident angle β is expressed

as [28]:

$$\sin\beta = m\sin\alpha \tag{4.15}$$

where $\beta = 3\alpha$. This means that the angle of the incident light to the the normal of the tangential plane has to be three times larger than the refracted angle. Thus gives the limit of the refracted angle of $\alpha \leq 30^o$, since the maximum angle of the incident light is 90^o. This also means that the lowest refractive index of which a triangular orbit may appear is $m = 2$. This limiting case of the triangular orbit is shown in figure 4.3 **d**. The path length of the ray inside the sphere can be expressed in terms of only the refractive index m and the sphere radius a [28]:

$$l = 6a\cos\alpha = 3a\sqrt{1+m} \tag{4.16}$$

This triangular orbit is expected to have a peak in the Fourier transform at $L = ml$, fully expressed as [28]:

$$L = m3a\sqrt{1+m} \tag{4.17}$$

Orbits with 4, 6, 8, ... bounces inside the sphere may also exist. The refractive index these orbits need enter the sphere by refraction is defined by [28]:

$$\sin((b+1)\alpha) = m\sin\alpha \tag{4.18}$$

Where $b = 2,\ 4\ , 6\ , ...$ is the number of bounces and α is the refracted angle relative to the normal of the tangential plane. When the number of bounces increase, the orbits converge to "whispering gallery" modes, which are modes of totally internally reflected rays that runs along the inside boundary of the sphere [28].

As seen in the various plots of the Q_{ext}-curve, the ripples seem to have a periodic nature with different shape and frequency. A reasonable analytic step is to take the Fourier transform (FT) of Q_{ext}. This will order the ripples in terms of frequency, thus separating ripples originating from different orbits. The Fourier transform is done by MATLAB's built in function for the Fast Fourier Transform (FFT)-algorithm.

4.3.1 The Fourier transform

The Fourier transform contains the amplitudes of the frequencies of sine and cosine functions which need to be superposed to recreate the original function. The continuous Fourier transform is defined as [30]:

$$F(\omega) = \frac{1}{\sqrt{2\pi}}\int_{-\infty}^{\infty} Q(k)e^{-i\omega k}dk \tag{4.19}$$

where $F(\omega)$ is a function of the harmonic frequencies ω which reconstruct the original function. $Q(k)$ is the original function (in this case Q_{ext}).

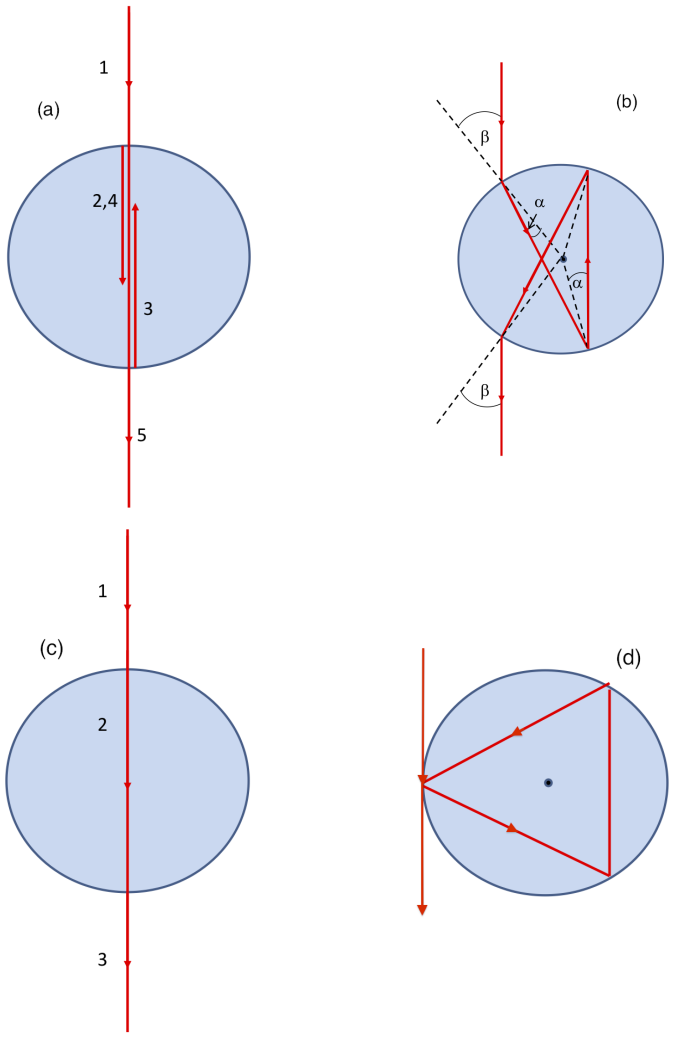

Figure 4.3: **a**: The diameter orbit, where the ray bounces two times off the inside boundary of the sphere, exiting the sphere in the incident direction (one dimensional scattering). **b**: The triangular orbit with refractive index $m > 2.0$, where $\beta = 3\alpha$, and is the incident angle relative to the normal of the tangent plane and α is the angle of the refracted ray relative to the normal of the tangent plane. **c**: Transmitted ray through the centre of the sphere, with 1/3 of the path length of the ray in **a**. **d**: Triangular orbit where the entrance and exit point is the same; at the limit of total internal reflection ($m = 2.0$). [28]

The FFT is an efficient way of doing a Discrete Fourier Transform (DFT), which is the way to do a Fourier transform numerically. The DFT is given in the following way [30]:

$$F(j) = \frac{1}{N} \sum_{j=0}^{N-1} Q(k) e^{-i2\pi jk/N} \tag{4.20}$$

where $j = 0,\ 1,\ ,\ ..., N-1$ and $k = 0,\ 1,\ ..., N-1$. The function $Q(k)$ is, as in the continuous version (eq. 4.19), projected onto a subspace of sine and cosine functions with an integer number of wavelengths between $j = 0$ and $j = N$. Since the sine (and cosine) functions with different integer number of wavelengths are mutually orthogonal, the subspace is an orthogonal basis for the function $Q(k)$. This means that any function $Q(k)$ can be projected onto this subspace if N is large enough, and the amplitude of the sine and cosine functions will determine the contribution to each frequency component of the subspace. The index j determines the frequency of the sine and cosine functions. The contribution $Q(k)$ makes to each of the frequencies j, is stored in the function $F(j)$. When analyzing the ripples in the Q_{ext}-curve this comes in handy to determine the periodicity, which is believed to be related to the path length of the rays inside the sphere.

The x-axis in the FT-diagrams is in units cm, which is the reciprocal of the wavenumber ($1/\tilde{\nu}$ $[cm]$). The y-axis shows the amplitude of the frequency in question, scaled against the largest amplitude in the FT-digram.

4.3.2 The Fourier transform of ADA

The first step is to take the Fourier transform of the Q_{ext}-curve of the anomalous diffraction approximation (ADA). This approximation shares the broad oscillations in the exact solution, but has none of the high frequent ripples and wiggles found in the real solution (shown in fig. 3.3). The diameter of the sphere is $13\mu m$, and its refractive index is 2.5. The Q_{ext}-curve is calculated by eq. 3.10, and Fourier transformed. The contribution from the constant 2 in 3.10, would lead to a large peak at zero in the FFT-plot. To eliminate this contribution the constant 2 is subtracted from the Q_{ext} curve. Figure 4.4 shows the squared absolute value of the result. The peak is at $1,95 \cdot 10^{-3}$ cm, which is not surprising since this is the wavenumber dependent phase lag defined by van de Hulst as $\rho = 2ka(m-1)$, which is the phase lag suffered by the central ray going through the sphere (fig. 4.3 **c**). The phase lag ρ also is the argument of the sine and cosine parts of 3.10. For this particular sphere the phase lag is $\rho = 1,95 \cdot 10^{-3} \cdot k$ (cm). The peak changes position with changing refractive index m and sphere size a according to the formula for ρ. Since the real solution show the same broad oscillations (fig. 3.10), this peak is also expected to be in the Fourier transform of the exact solution.

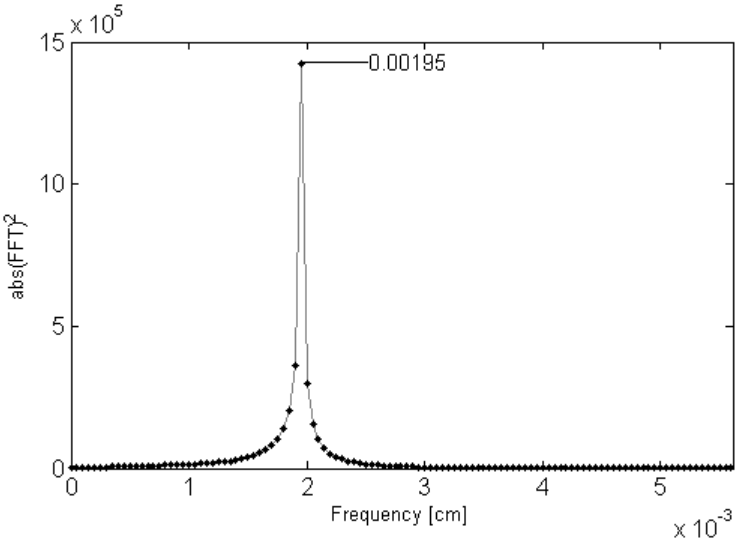

Figure 4.4: Shows the Fourier transform of Q_{ext} made from ADA with $a = 6.5\mu m$ and $m = 2.5$, with the frequency of the oscillations in Q_{ext} calculated by ADA.

4.3.3 The Fourier transform of the exact solution

In the exact solutions the high frequent wiggles are present, and will be represented as peaks with a higher frequency in the Fourier transform than those originating from the phase lag. The Q_{ext}-curve is calculated with the same size of the sphere as the last section, $a = 6.5\mu m$ and different refractive indices. To eliminate the large amplitude at zero in the FT diagram a constant 2.3 is subtracted from the Q_{ext}-curve, since this is approximately the value the curve oscillates about.

Figure 4.5 shows the Fourier transform of Q_{ext} radius $a = 6.5\mu m$ and refractive index $m = 1.33$. The figure also shows two plots of Q_{ext} for the sphere in different ranges of the size parameter x. The plot with low x-values shows none of the sharp ripples, while the plot of Q_{ext} with higher values of x shows the sharp ripple structure. The first and largest peak is expected to be at $\rho/k = 2a(m-1) = 0.00043\ cm$, but since the step size is $0.00005cm$ the peak appears at $0.0004cm$. The triangular orbit, if present, would according to 4.17 have a peak at $\sim 0.004cm$. Fig. 4.5 does not show a peak here. The closest peak is at $0.0049cm$, which is closer to the diameter orbit, expected to be at $3 \cdot 0.0013 \cdot 1.33 = 0.0052cm$. The small peaks at $0.01cm$ and $0.01495cm$ correspond to approximately integer multiples of the second peak, meaning that they probably correspond to the same orbit at the first peak, but are running two and three times around the orbit, suffering phase lags two and three

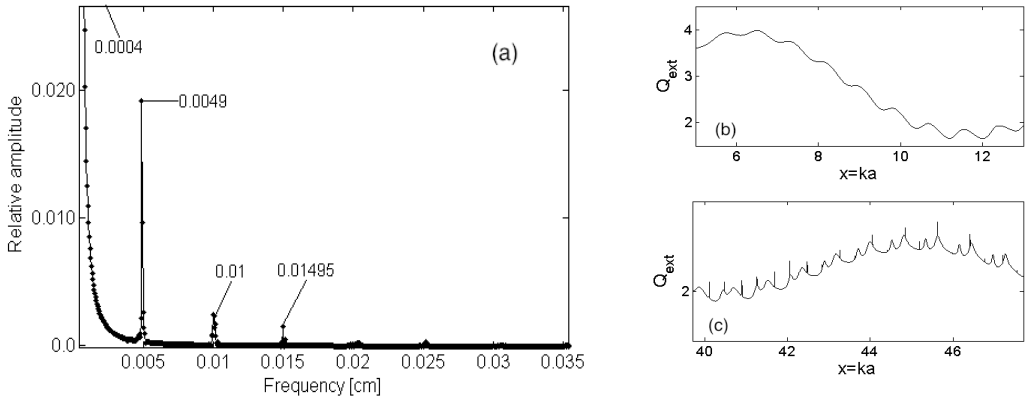

Figure 4.5: **a**: Fourier transform of Q_{ext} calculated by the exact solution of a sphere with radius $a = 6.5\mu m$ and refractive index $m = 1.33$, with the relative amplitude on the y-axis and frequency of the ripples and oscillations in Q_{ext} on the x-axis. **b**: Excerpt from the whole Q_{ext}-curve of the sphere showing the ripples and broad oscillations. **c**: Excerpt from the whole Q_{ext}-curve of the sphere showing the ripples and broad oscillations with larger size parameter x than **b**.

times as large as the orbit running once around the orbit.

Figure 4.6 shows the Fourier transform of Q_{ext} from a sphere with refractive index $m = 1.8$ and radius $a = 6.5\mu m$. Apart from the expected peak at $0.00104cm$, the diagram shows a relatively large second peak at $0.0061cm$. This is a little larger than the resonant triangular orbit expected at $0.0058cm$. The third and fourth peak is approximately an integer multiple of the second one, as in the previous case.

Figure 4.7 shows the FT-diagram and an extract from the Q_{ext}-curve of the exact solution of a sphere with the same size as the previous and with a refractive index $m = 2.0$. The a second peak is located at 0.0675, which is the expected location of the triangular orbit. The relative amplitude of the second peak is about twice as high as in fig. 4.6. The second peak, believed to originate from the triangular orbit, increases in relative amplitude with refractive index, and with a refractive index of 2.4 the second peak exceeds the phase lag peak described is sec. 4.3.2 and becomes the most important contribution to the variation in Q_{ext}.

In figure 4.8 the Fourier transform of Q_{ext} from the exact solution, with increasing refractive indices, is shown. The peaks generally show a trend where increasing refractive index gives an increasing amplitude of the peak. The group of peaks showing the largest amplitudes in the figure, all have a value on the x-axis of $\sim m \cdot 0.0039\ cm$,

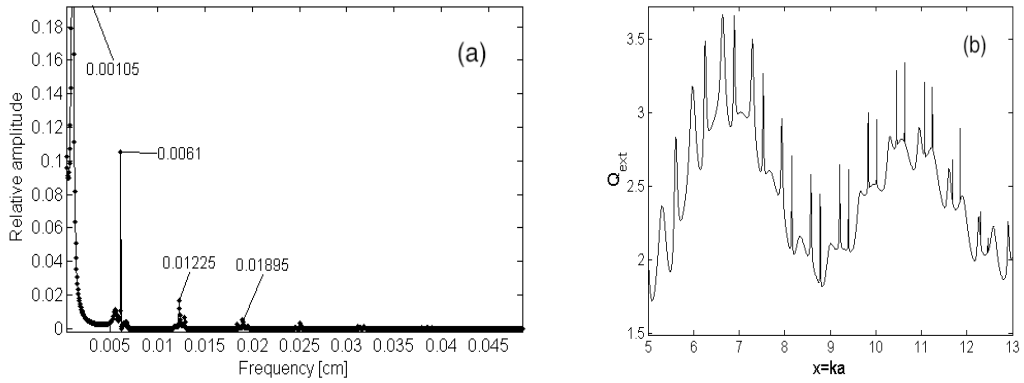

Figure 4.6: **a**: Fourier transform of Q_{ext} calculated by the exact solution of a sphere with radius $a = 6.5\mu m$ and refractive index $m = 1.8$, with the relative amplitude on the y-axis and frequency of the ripples and oscillations in Q_{ext} on the x-axis. **b**: Excerpt from the whole Q_{ext}-curve of the sphere, showing ripples and broad oscillations.

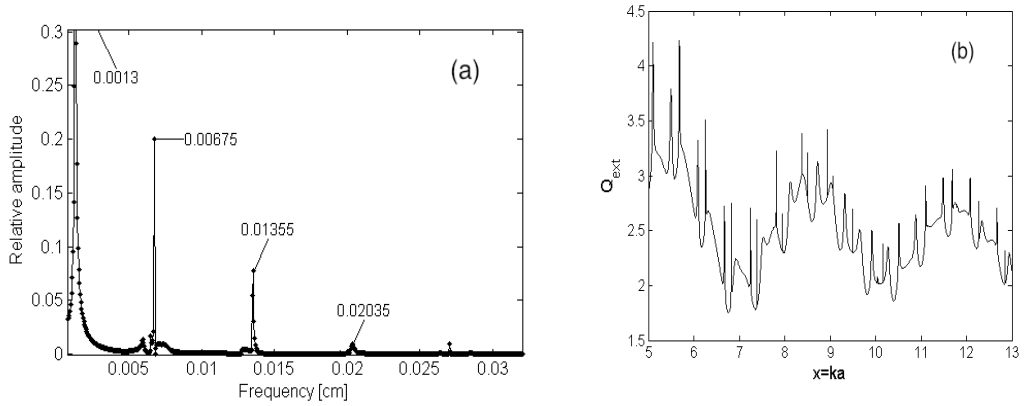

Figure 4.7: **a**: Fourier transform of Q_{ext} calculated by the exact solution of a sphere with radius $a = 6.5\mu m$ and refractive index $m = 2.0$, with the relative amplitude on the y-axis and the frequency of the ripples and oscillations in Q_{ext} on the x-axis. **b**: An excerpt from the whole Q_{ext}-curve of the sphere, showing ripples and broad oscillations.

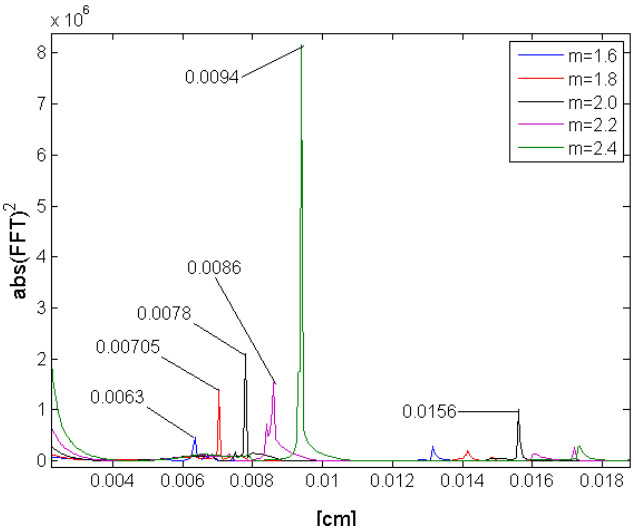

Figure 4.8: The Fourier transform of Q_{ext} calculated by the exact solution, with refractive indices $m = 1.6$, $m = 1.8$, $m = 2.0$, $m = 2.2$ and $m = 2.4$. The sphere used in the calculations has a radius $a = 7.5\mu m$

where m is the refractive index. Only the line showing a peak at 0.0078, which represent the refractive index $m = 2.0$ and radius $a = 7.5\mu m$, have a value on the x-axis exactly equal to 0.0039 cm. This is the exact path length predicted by equation 4.16, and is also the lowest refractive index at which this orbit can be obtained by refraction. None of the other peaks fit the prediction of the path length made by equation 4.16, with their respective refractive index used in the equation.

The peak at the x-value 0.0156 in figure 4.8 also belongs to the sphere with $m = 2.0$, and is the first multiple of the peak at 0.0078. The peak at 0.0078 is perfectly predicted by equation 4.17, and can be explained by rays undergoing a triangular orbit. The peak at 0.0156 can be explained by rays undergoing a second lap around the orbit before leaving the sphere. At $m = 2.0$ the entrance point of the ray is the same as the exit point (fig. 4.3 **d**). Rays reflecting five times inside the sphere will have made two laps around the orbit, with twice the path length l (eq. 4.16). The triangular orbit at $m = 2.0$ is a at the limit of total internal reflection, which corresponds to the limit where rays can enter the sphere via refraction.

The largest peak in figure 4.8 is from the FFT-line from Q_{ext} with $m = 2.4$. At this refractive index the triangular orbit is realizable by refraction, which makes it reasonable that this peak is much larger than the others. The peak one would expect in the region near the second peak of the $m = 2.0$ FT-line, is nearly non-existing. This can be explained by the entrance point not being in the same place as the exit

point. Which means that a ray undergoing five bounces will not leave the sphere in direction of the incident ray.

4.3.4 The Fourier transform of Q_{NA}

The plots in figure 3.9 and 3.10 show similar type of ripple structure as the Q_{ext}-curves of figure 4.1. The origin of these ripples are most likely much more complex than the origin of the ripples in Q_{ext}, since the orbits causing these ripples will leave the sphere in an interval of angles relative to the incident direction. Therefore, an attempt to explain the results of this section will be futile within the scope of this thesis.

The data used to plot the exact and approximated Q_{NA}-curves of section 3.4.1 are Fourier transformed using the FFT-algorithm in MATLAB as described earlier in this section. The exact solution and the approximation are plotted in the same figure to compare the tops.

As seen in figure 4.9 the peaks in the Fourier transform of the exact and approximated Q_{NA} coincide on the x-axis, but the amplitude is larger for the approximation.

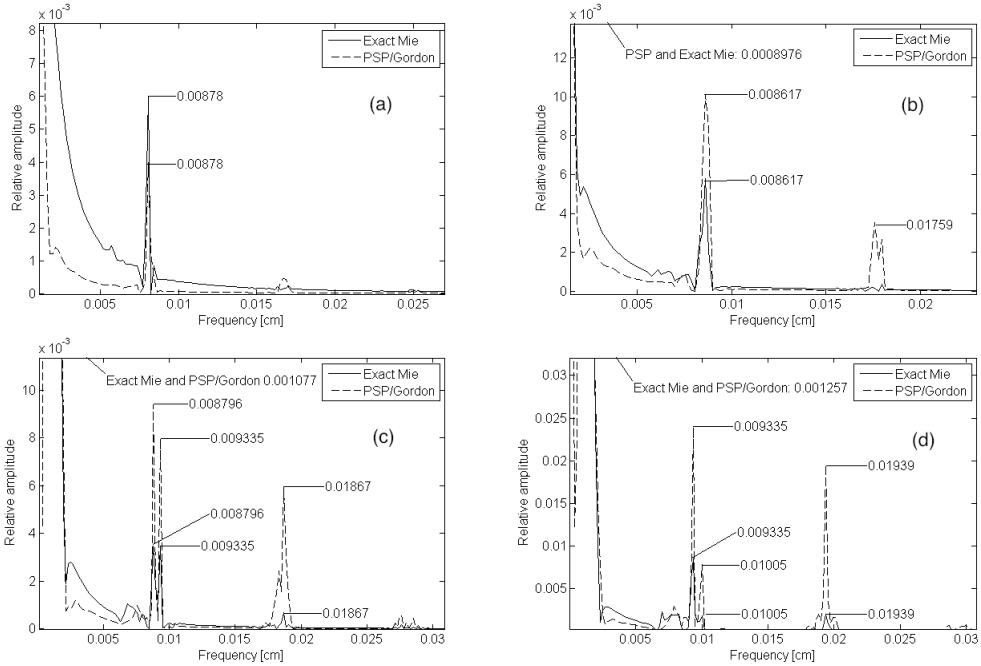

Figure 4.9: The Fourier transforms of efficiency Q_{NA} with $\theta_{\mathrm{NA}} = 35^o$ and different values of the refractive index m. The striped lines show Q_{NA} calculated the exact solution, and the solid lines show Q_{NA} calculated by the PSP and Gordon approximation. **a**: $m = 1.3$, **b**: $m = 1.4$, **c**: $m = 1.5$, **c**: $m = 1.6$

5 Discussion and conclusions

5.1 Approximations to the exact solution

In this thesis different approximations with different regions of validity in terms of angle of size parameter has been tested. In section 3.4.1 the approaches presented are meant for integrations of a relatively large range of angles θ. The integration is done for the range $\theta = 0^o$ to $\theta_{\mathrm{NA}} = 35^o$. This range is used since it corresponds to the value of NA in standard FTIR microscopes. In addition to being the value of NA used in the example in section 3.13. Since the pattern of the Mie scattering is very different at angles near the forward direction ($\theta \sim 0$), it is hard to find approximations that are valid both for small and large angles. Two of the approaches evaluated in section 3.4.1 employ two different approximations in the integrations, the PSP or FM approximation for small angles ($\leq 10^o$) and the Gordon approximation for larger angles ($> 10^o$). The plots in figures 3.9, 3.10 and 3.11 show that the approaches using two different approximations performs much better than the ones were one approximation is used.

The intensity of the scattered light is about an order of magnitude larger near the forward direction, which can be seen from figures 3.6, 3.7 and 3.8. This means the lower angels are more important than the larger ones. Thus, the approximation in the forward direction will perform reasonably well, even if it is combined with the approximations that is less accurate at larger angles. This is shown in the plots in figure 3.9. At large values of θ and large values of x, non of the approximations perform very well. Integrations excluding the near forward angles is therefor not expected to perform as well as the ones including the near forward direction 3.4.1.

The difference between the FM and PSP approximation is the two functions f_1 and f_2 (eq. 3.21 and 3.22). These functions are multiplied with the PSP approximation in discontinuous intervals dependent of the size parameter x. This extension is made as an improvement of the PSP approximation, but does not improve the integrations made in section 3.4.1. In fact the unmodified PSP approximation performs slightly

better. Neither does it contain the discontinuities induced by switching on and off of the functions f_1 and f_2, which one could imagine would be a disturbance when correcting spectroscopic data. The combination of the PSP approximation and the Gordon approximation is found to give the best approximation to the exact value of Q_{NA}, with $\theta_{\mathrm{NA}} \leq 35$.

The combination of the PSP and Gordon approximation is applied in the example given in section 3.13. The example shows that the Mie scattering estimated by the approach in section 3.4.1 can be justified to give the scattering contribution to the spectrum from the pollen grain. The only unknown parameter is the refractive index, which in the example seemed to fit the best for $m = 1.31$. This is might be a little low, but is not far off from refractive indices measured in other biological particles and pollen of other species [24, 25].

5.2 The ripple stucture

In chapter 4 the ripples in the exact Mie solution is analyzed. The problem of particle scattering of at square potential is solved using quantum mechanics, and is shown to be equivalent with the solving of the one dimensional case of light scattering at a medium of different refractive index. This motivates using a semiclassical approach to the scattering problem, where the light is viewed as rays which correspond to the bound states of the quantum mechanical case. If this ray picture is applicable to two and three dimensional problems, ray dynamics can be used to explain the resonances giving the ripples in Q_{ext}. The resonances will correspond to rays going in orbits inside the sphere, entering and exiting the sphere in the same direction.

In section 4.3 the Q_{ext}-curve calculated by the exact solution is Fourier transformed to give the signatures of the ripples. This is done in an attempt to connect the ripples with the rays. From ray dynamics, the path lengths of the orbits in the sphere can be calculated. The orbits obtainable by refraction follow Snell's law, thus giving simple formulas for predicting the path length and location in the Fourier transform. At a refractive index $m = 2.0$ a triangular orbit is obtainable (fig. 4.3 **d**). The analysis in section 4.3 focuses on the triangular orbit.

Figure 4.8 shows that the first peak increases in amplitude with increasing refractive index. The plot shows that the first peaks move towards higher frequency with increasing refractive index. The location of the peaks are well but not perfectly predicted by ray dynamics, except for the refractive index $m = 2.0$, where the peak is perfectly predicted. The second peak on the Fourier transform in figure 4.8 is much larger for $m = 2.0$ than for the curves representing other refractive indices, even the ones with refractive index larger than $m = 2.0$. Since $m = 2.0$ is the only refractive

index for which the triangular orbit can go twice around the sphere, and end up in the direction of the incident light, it is natural that $m = 2.0$ is the only refractive index with a significant contribution on the second peak. The relatively large first peak in the Fourier transform for $m = 2.4$ is expected, since the triangular orbit is an "open channel" at this refractive index. From this the conclusion can be drawn that the triangular orbit has signatures in the Fourier transform of Q_{ext} is to a high degree as expected from ray dynamics. The ripples in Q_{ext} analyzed in section 4.3 is therefore likely to be connected with the triangular orbit.

The Fourier transforms in section 4.3 shows signatures of the triangular orbit for lower values of the refractive index than $m = 2.0$. For $m < 2.0$ the triangular orbit corresponds to a "closed channel", which is not obtainable by refraction, since they by the localization principle miss the sphere (sec. 4.2.3). These orbits are not analyzed in this thesis.

5.3 the extinction paradox - some consequences

The extinction paradox is not discussed earlier in this thesis, even though it is well examined in the literature [11, 18]. The reason for this is that it does not interfere with the use of the Mie solutions in theory, but might become a problem in practical applications.

In section 3.1 the extinction efficiency Q_{ext}, based on the exact solution, was calculated and plotted. The extinction efficiency is the extinction cross section divided by the geometrical cross section, with the extinction cross section being the area of the incident beam one has to cover up to account for the scattered and absorbed light. A natural assumption to make is that the extinction cross section cannot be larger than the area of the geometrical cross section of the sphere, which in case would correspond to an opaque disk, and an extinction efficiency $Q_{ext} = 1$. As we see in section 3.1, and maybe even more explicitly in figure 3.3, this is not the case. The extinction efficiency is in many cases much larger, and seem to oscillate around a value of about about 2. This is called the extinction paradox [11].

When applying infrared spectroscopy to analyze a spherically shaped object, the transmission T is defined in chapter 2.5 (eq. 2.42) as the transmitted light divided by the incident light. This definition is equivalent with the other definition, in the same section, (eq. transmission) which defines the transmission as $T = 1 - Q_{ext}$, which will often give a transmission of less than zero. This proposes a problem when calculating the absorbance A (eq. 2.43), defined as $A = -\log_{10}(T)$, since the logarithm of a negative number is not possible.

The physical interpretation of the scattering paradox is that the scattering from a sphere can be divided into two parts: A refraction part and a diffraction part. The refraction part is the light redirected by entering and leaving the sphere, and is the scattering originating from the light which hits the geometrical cross section of the sphere. The diffraction part is the light which is diffracted at the edge of the sphere, and forms a diffraction pattern as from a circular hole, according to Babinet's principle. This idea is the basis of the anomalous diffraction approximation in section 3.2.1. [11]

The extinction paradox may also be seen through the semiclassical ray picture introduced in section 4.2.3. The rays which have an angular momentum lower than l_{max}, where l_{max} correspond to the angular momentum which by the localization principle (sec. 4.2.3) equals the radius of the sphere, is the rays contributing to the refraction part of the scattering. The rays with angular momentum larger than l_{max} is the rays contributing to the diffraction part of the scattering. [13]

5.4 Future work

To be able to properly correct IR-spectra distorted by Mie scattering, more extensive methods than than in section 3.13 need to be developed. A similar approach as the Extended Multiplicative Signal Correction (EMSC) [10] mentioned in the introduction, might be developed to estimate the Mie scattering contribution with a numerical aperture.

The ripples in Q_{ext} needs to be more thoroughly examined to link the orbits to the peaks in the Fourier transform. In this thesis only the classically obtainable orbits are addressed, and the location of the whispering gallery modes in the Fourier transform diagram is not discussed. Future work should also include ways to predict the amplitude of the ripples in Q_{ext} by means of ray dynamics. This is already done by semiclassical means [26, 31, 32].

Bibliography

[1] P. Bassan, A. Kohler, H. Martens, J. Lee, E. Jackson, N. Lockyer, P. Dumas, M. Brown, N. Clarke, and P. Gardner, "Rmies-emsc correction for infrared spectra of biological cells: Extension using full mie theory and gpu computing," *Journal of Biophotonics*, vol. 3, April 2010.

[2] P. Bassan, A. Kohler, H. Martens, J. Lee, H. J. Byrne, P. Dumas, E. Gazi, M. Brown, N. Clarke, and P. Gardner, "Resonant mie scattering (rmies) correction of infrared spectra from highly scattering biological samples," *Analyst*, vol. 135, no. 2, 2009.

[3] B. J. Davis, P. S. Carney, and R. Bhargava, "Theory of midinfrared absorption microspectroscopy: I. homogeneous samples," *Analytical Chemistry*, vol. 82, May 2010.

[4] B. J. Davis, P. S. Carney, and R. Bhargava, "Theory of midinfrared absorption microspectroscopy for intact fibers," *Analytical Chemistry*, vol. 83, January 2011.

[5] B. Mohlenhoff, M. Romeo, M. Diem, and B. R. Wood, "Mie-type scattering and non-beer-lambert absorption behaviour of human cells in infrared microspectroscopy," *Biophysical Journal*, vol. 88, 2005.

[6] C. P. S. Hsu, *Infrared Spectroscopy.* Prentice Hall, Inc., 1. ed., 1997.

[7] D. H. Bilderback, P. Elleaume, and E. Weckert, "Review of third and next generation synchrotron light sources," *Journal of Physics B: Atomic, Molecular and Optical Physics*, vol. 38, January 2005.

[8] P. Bassan, H. J. Byrne, F. Bonnier, J. Lee, P. Dumas, and P. Gardner, "Resonant mie scattering in infrared spectroscopy of biological materials - understanding the "dispersion artefact"," *Analyst*, May 2009.

[9] A. Kohler, U. Böcker, J. Warringer, A. Blomberg, S. W. Omholt, E. Stark, and H. Martens, "Reducing inter-replicate variation in fourier transform infrared

spectroscopy by extended multiplicative signal correction," *Applied Spectroscopy*, vol. 63, no. 3, 2009.

[10] A. Kohler, J. Sulé-Suso, G. D. Sockalingum, M. Torbin, F. Bahrami, Y. Yang, J. Pijanka, P. Dumas, M. Cotte, D. G. van Pittius, G. Parkes, and H. Martens, "Estimating an correcting mie scattering in synchrotron-based microscopic fourier transform infrared spectra by extended multiplicative signal correction," *Applied Spectroscopy*, vol. 62, no. 3, 2008.

[11] H. C. van de Hulst, *Light Scattering by Small Particles*. Dover Publications Inc., 1957, 1981.

[12] W. J. Wiscombe, "Improved mie scattering algorithms," *Applied Optics*, vol. 19, May 1980.

[13] R. Blümel, "Mie-notes." Unpubllished notes on Mie-scattering, March 2013.

[14] A. L. Fymat and K. D. Mease, "Mie forward scattering: improved semiempirical approximation with application to particle size distribution inversion," *Applied Optics*, vol. 20, January 1981.

[15] J. E. Gordon, "Simple method for approximating mie scattering," *Journal of the Optical Scociety of America*, vol. 2, February 1985.

[16] A. Kohler and R. Blümel, "Scattering and absorption of infrared light at absorbing thin films and spheres: A exact description of the absorbance spectrum." Unpublished article.

[17] D. J. Griffiths, *Introduction to Electrodynamics*. Prentice Hall, Inc., 2. ed., 1989.

[18] C. F. Bohren and D. R. Huffman, *Absorption and Scattering of Light by Small Particles*. Wiley-VCH, 2004.

[19] C. Mätzler, "Matlab functions for mie scattering and absorption," tech. rep., University of Bern, June 2002.

[20] A. Ishimaru, *Wave Propagation and Scattering in Random Media*. IEEE Press and Oxford University Press, 1997.

[21] L. M. Miller and P. Dumas, "Chemical imaging of biologival tissue with synchrotron infrared light," *Biochimica et Biophysica Acta*, vol. 1758, pp. 846–856, April 2006.

[22] R. B. Penndorf, "Approximation formula for forward scattering," *Journal of the Optical Scociety of America*, vol. 52, July 1962.

[23] K. Shimizu, "Modification of the rayleigh-debye approximation," *Journal of the Optical Scociety of America*, vol. 73, April 1983.

[24] J. Beuthan, O. Mient, J. Helfmann, M. Herring, and G. Müller, "The spatial variation of the refractive index in biological cells," *Phys. Med. Biol.*, vol. 41, no. 369, 1996.

[25] M. Ebert, S. Weinberg, A. Rausch, G. Gorzawski, P. Hoffmann, H. Wex, and G. Helas, "Complex refractive index of aerosols during lace 98 as derived from the analysis of idividual particles," *Journal of Geophysical Research*, vol. 107, no. D21, 2002.

[26] H. M. Nussenzveig, *Diffraction Effects in Semiclassical Scattering*. Cambridge University Press, 1992.

[27] P. W. Barber and R. K. Chang, eds., *Optical Effects Associated With Small Particles*. No. 1 in Advanced Series in Applied Physics, World Scientific, 1988.

[28] A. Kohler and R. Blümel, "Semi-classical approximation formulae for the scattering of light at soft paricles." Unpublished notes, April 2013.

[29] B. Simons, "Advanced quantum physics," March 2013. Lecture notes: http://www.tcm.phy.cam.ac.uk/ bds10/aqp/handout_1d.pdf.

[30] A. I. Vistnes, *Svingninger og Bølger*. Universitetet i Oslo, 2012.

[31] R. Blümel and U. Smilansky, "A simple model for chaotic scattering," *Physica D*, vol. 36, January 1989.

[32] K. W. Ford and J. A. Wheeler, "Semiclassical description of scattering," *Annals of Physics*, vol. 7, 1959.

[33] E. Kreyzsig, *Advanced Engineering Mathematics*. John Wiley & sons, inc., 9th ed., 2006.

[34] K. Rottmann, *Matematisk Formelsamling*. Spektrum forlag, 2003.

A Formulas

A.1 Mie equations and coefficients

The function $\pi(\cos\theta)$ used to calculate the amplitude functions $S(\theta)$ [11]:

$$\pi(\cos\theta) = \frac{1}{\sin\theta}P_n^1(\cos\theta) = \frac{1}{\sin\theta}(1-\cos^2\theta)^{1/2}\frac{d}{d\cos\theta}P_n(\cos\theta) = \frac{d}{d\cos\theta}P_n(\cos\theta) \tag{A.1}$$

The function $\tau(\cos\theta)$ expressed in terms of $\pi_n(\cos\theta)$ [11]:

$$\tau_n(\cos\theta) = \cos\theta\cdot\pi_n(\cos\theta) + (\cos^2\theta - 1)\frac{d}{d\cos\theta}\pi_n(\cos\theta) \tag{A.2}$$

The coefficients for the internal field c_n and d_n are given as [18]:

$$c_n = \frac{\mu_1 j_n(x)[xh_n^{(1)}(x)]' - \mu_1 h_n^{(1)}(x)[xj_n(x)]'}{\mu_1 j_n(mx)[xh_n^{(1)}(x)]' - \mu h_n^{(1)}(x)[mxj_n(mx)]'} \tag{A.3}$$

and:

$$d_n = \frac{\mu_1 m j_n(x)[xh_n^{(1)}(x)]' - \mu_1 m h_n^{(1)}(x)[xj_n(x)]'}{\mu m^2 j_n(mx)[xh_n^{(1)}(x)]' - \mu_1 h_n^{(1)}(x)[mxj_n(mx)]'} \tag{A.4}$$

where μ_1 is the magnetic permeability of the sphere, μ is the magnetic permeability of the ambient medium, m is the refractive index, x is the size parameter. The

The scalar vector wave components m_n and n_n is given as [19].

$$m_n = \int_{-1}^{1}(m_\theta + m_\phi)d(\cos\theta) = 2(2n+1)|j_n(z)|^2 \tag{A.5}$$

And:

$$n_n = \int_{-1}^{1}(n_r + n_\theta + n_\phi)d(\cos\theta) = 2n(2n+1)\left[(n+1)\left|\frac{j_n(z)}{z}\right|^2 + \left|\frac{(zj_n(z))'}{z}\right|^2\right] \tag{A.6}$$

where $z = mrk$, m is the refractive index, k is the wavenumber and r is the distance from the center of the sphre $(0 < r < a)$

A.1.1 Incident and scattered wave in spherical coordinates

The incident plane wave in spherical coordinates [11]:

$$u = e^{i\omega t}\cos\phi\sum_{n=1}^{\infty}(-i)^n\frac{2n+1}{n(n+1)}P_n^1(\cos\theta)j_n(kr) \tag{A.7}$$

$$v = e^{i\omega t}\sin\phi\sum_{n=1}^{\infty}(-i)^n\frac{2n+1}{n(n+1)}P_n^1(\cos\theta)j_n(kr) \tag{A.8}$$

The scattered wave in spherical coordinates [11]:

$$u = e^{i\omega t}\cos\phi\sum_{n=1}^{\infty}-a_n(-i)^n\frac{2n+1}{n(n+1)}P_n^1(\cos\theta)h_n^{(2)}(kr) \tag{A.9}$$

$$v = e^{i\omega t}\sin\phi\sum_{n=1}^{\infty}-b_n(-i)^n\frac{2n+1}{n(n+1)}P_n^1(\cos\theta)h_n^{(2)}(kr) \tag{A.10}$$

The inside wave in spherical coordinates [11]:

$$u = e^{i\omega t}\cos\phi\sum_{n=1}^{\infty}m\ c_n(-i)^n\frac{2n+1}{n(n+1)}P_n^1(\cos\theta)h_n^{(2)}(mkr) \tag{A.11}$$

$$v = e^{i\omega t}\sin\phi\sum_{n=1}^{\infty}m\ d_n(-i)^n\frac{2n+1}{n(n+1)}P_n^1(\cos\theta)h_n^{(2)}(mkr) \tag{A.12}$$

where ϕ and θ are the azimuth and scattering angle shown in figure 2.2, the function $P_n^1(\cos\theta)$ is the associated Legendre polynomial, and $j_n(kr)$ is the spherical Bessel function.

A.2 Legendre polynomials

The Legendre polynomial $P_n(\cos\theta)$ [33]:

$$P_n(\cos\theta) = \sum_{m=0}^{M}(-1)^m\frac{(2n-2m)!}{2^n m!(n-m)!(n-2m)!}\cos^{n-2m}\theta \tag{A.13}$$

Where $M = n/2$ or $(n-1)/2$, whichever is an integer.

The associated Legendre polynomial is related to the Legendre polynomial through [34]:

$$P_n^m(x) = (1-x^2)^{m/2}\frac{d^m}{dx^m}P_n(x) \tag{A.14}$$

A.3 Bessel functions

The spherical Bessel function is related to the Bessel function by [34]:

$$j_n(z) = \sqrt{\frac{\pi}{2z}} J_{n+1/2}(z) \tag{A.15}$$

The first kind of Bessel function is given by [34]:

$$J_{n+1/2}(z) = \left(\frac{z}{2}\right)^{n+1/2} \sum_{l=0}^{\infty} \frac{(iz/2)^{2l}}{l!\ \Gamma(n+l+3/2)} \tag{A.16}$$

where the gamma function $\Gamma(x)$ is given by:

$$\Gamma(x) = \left[x e^{Cx} \prod (1 + x/n) e^{-x/n} \right]^{-1} \tag{A.17}$$

C is the Euler constant $\simeq 0.577215$.

The Hänkel function is given by [34]:

$$H_n^{(2)}(z) = J_n(z) - iN_n(z) = J_n(z) - \frac{i}{\sin(n\pi)} [\cos(n\pi) J_n(z) - J_{-n}(z)] \tag{A.18}$$

The spherical Hänkel function [34]

$$h_n^{(2)}(z) = \sqrt{\frac{\pi}{2z}} H_n^{(2)}(z) \tag{A.19}$$

A.4 Spherical harmonics

Scalar wave equation in spherical coordinates [18]

$$\frac{1}{r^2}\frac{\partial}{\partial r}\left(r^2 \frac{\partial \psi}{\partial r}\right) + \frac{1}{r^2 sin\theta}\frac{\partial}{\partial \theta}\left(\sin\theta \frac{\partial \psi}{\partial \theta}\right) + \frac{1}{r^2 sin\theta}\frac{\partial^2 \psi}{\partial \phi^2} + k^2 \psi = 0 \tag{A.20}$$

Jackson spherical harmonics [13]:

$$Y_{lm}(\theta, \phi) = \sqrt{\left(\frac{2l+1}{4\pi}\right)\frac{(l-m)!}{(l+m)!}} P_l^m(\cos\theta) e^{im\theta} \tag{A.21}$$

where $P_l^m(\cos\theta)$ is the associated legendre polynomials.

A.4.1 Vector spherical harmonics

$$\begin{aligned} \mathbf{M}_{emn} &= \nabla \times (r\psi_{emn}) \\ \mathbf{N}_{emn} &= \frac{\nabla \times \mathbf{M}_{emn}}{k} \\ \mathbf{M}_{omn} &= \nabla \times (r\psi_{omn}) \\ \mathbf{N}_{omn} &= \frac{\nabla \times \mathbf{M}_{omn}}{k} \end{aligned} \tag{A.22}$$

Where $\psi_{emn} = \cos(m\phi)P_n^m(\cos\phi)z_n(kr)$ and $\psi_{omn} = \sin(m\phi)P_n^m(\cos\phi)z_n(kr)$. The subscript e and o denotes even and odd solutions. The function z_n is any of the spherical Bessel functions and $n = m, m+1, \ldots$.

A.5 Wiscombe´s approximation

Formulas for Q_{ext} and Q_{sca} [12]:

$$Q_{ext} = 6xRe\left(\hat{a}_1 + \hat{b}_1 + \frac{5}{2}\hat{a}_2\right) \tag{A.23}$$

And:

$$Q_{sca} = 6x^4T \tag{A.24}$$

$$S_1(\cos\theta) = \frac{3}{2}x^3\left[\hat{a}_1 + \left(\hat{b}_1 + \frac{5}{3}\hat{a}_2\right)\cos\theta\right] \tag{A.25}$$

$$S_2(\cos\theta) = \frac{3}{2}x^3\left[\hat{b}_1 + \hat{a}_1\cos\theta + \frac{5}{3}\hat{a}_2(2\cos^2\theta - 1)\right] \tag{A.26}$$

The coefficients in Wiscombe´s approximation $\hat{a}_1$, $\hat{a}_2$, $\hat{b}_1$ and T are given as:

$$\hat{a}_1 = 2i\frac{(m^2-1)}{3}\frac{\left(1 - \frac{1}{10}x^2 + \frac{4m^2+5}{1400}x^4\right)}{D} \tag{A.27}$$

$$\begin{aligned} D = m^2 + 2 + \left(1 - \frac{7}{10}m^2\right)x^2 - \\ \frac{8m^4 - 385m^2 + 350}{1400}x^4 + 2i\frac{m^2-1}{3}x^3\left(1 - \frac{1}{10}x^2\right) \end{aligned} \tag{A.28}$$

$$\hat{b}_1 = ix^2\frac{(m^2-1)}{45}\frac{\left(1+\frac{2m^2-5}{70}x^2\right)}{\left(1-\frac{2m^2-5}{30}x^2\right)} \tag{A.29}$$

$$\hat{a}_2 = ix^2\frac{(m^2-1)}{15}\frac{\left(1-\frac{1}{14}x^2\right)}{\left(2m^2+3-\frac{2m^2-7}{14}x^2\right)} \tag{A.30}$$

$$T \equiv |\hat{a}_1|^2 + |\hat{b}_1|^2 + \frac{5}{3}|\hat{a}_2|^2 \tag{A.31}$$

Where is the complex refractive index $m = n + in'$ and $x = ka$

A.5.1 Derivation of ε_{rel} for Wiscombe's approximation

When $x \to 0$ the terms $\hat{b_1}$ and $\hat{a_2}$ goes to 0, since they both are multiples of x^2. The expression for Q_{ext} reduces to:

$$Q_{ext,W} = 6x\ Re(\hat{a}_1) \tag{A.32}$$

The term $\hat{a}_1$ reduces to:

$$\hat{a}_1 = 2i\frac{m^2-1}{3D} \tag{A.33}$$

since the rest are multiples of x^2 and x^4. The term D for similar reasons, reduces to $D = m^2 + 2$. The extinction efficiency now becomes:

$$Q_{ext,W} = 6x\ Re\left(\frac{m^2-1}{3m^2+6}\right) \tag{A.34}$$

The squared of the complex refractive index is $m^2 = n^2+2inn'+n'^2$. The denominator includes a complex number $((3n^2 - 3n'^2 + 6inn')$, which means we have to multiply over and under with the complex conjugate. Since we are only interested in the real part, only the real terms in the numerator is carried along.

$$\begin{aligned} Q_{ext,W} &= 6x\left(\frac{12n'n^3 - 12n'n^3 + 12nn'^3 - 24n'n12nn'^3 - 12n'n}{(3n^2-3n'^2+6)^2+36nn'}\right) \\ &= 6x\left(\frac{-36nn'}{9(n^2-n'^2+2)^2+36nn'}\right) = 6x\left(\frac{-4nn'}{(n^2-n'^2+2)^2+4nn'}\right) \\ &= \left(\frac{-24nn'}{n^4+n'^4-2(nn')^2+4n^2-4n'^2+4+4nn'}\right) \end{aligned} \tag{A.35}$$

The relative difference is defined in equation 3.15. Blümel's approximation [13] proves to converge to the real solution for $x \to 0$ in sec. 3.2.2. By using Blümels formula for

very small x (dropping terms which are multiples of x^2 and x^3), we can estimate the relative difference. Blümel's approximation for very small x is given as [13]:

$$Q_{ext,B} = \frac{6xnn'}{(nn')^2 + [1 + \frac{1}{2}(n^2 - n'^2)]^2} \tag{A.36}$$

By expanding the parenthesis and multiplying by 4 we get:

$$Q_{ext,B} = \frac{24xnn'}{4 + 4n^2 - 4n'^2 + n^4 + n'^4 + 2(nn')^2} \tag{A.37}$$

Now by defining the term $A = 4 + 4n^2 - 4n'^2 + n^4 + n'4$, the relative difference $\varepsilon_{rel} = (Q_{ext,B} - Q_{ext,W})/Q_{ext,W}$ becomes:

$$\lim_{x\to 0} \varepsilon_{rel} = \frac{\frac{24xnn'}{A+2(nn')^2} - \left(\frac{-24nn'}{A-2(nn')^2+4nn'}\right)}{\frac{24xnn'}{A+2(nn')^2}} = 1 + \frac{A + 2(nn')^2}{A - 2(nn')^2 + 4nn'} \tag{A.38}$$

B MATLAB CODE

B.1 Angle integration; calculating Q_{NA}

Listing B.1: Inegrate_angles.m

```
%This is a program that allows you to integrate any scattering property in
%a range of wavenumbers from 'k_min' to 'k_max', and over an intervall of
%angels theta from 'theta_min' to 'theta_max'. By integrating from
%'theta_min'=0 up to a 'theta_max' associated with a numerical aperture,
%Q_NA can be found.
%Wavenumber k = (2*pi*(1/lambda[cm]))[cm^-1].
%Wavenumber wn = (1/lambda[cm])[cm^-1]
%Uses the function 'Fymat_Mease.m' for calculation of the Fymat and Mease
%(FM) approximation and the Penndorf-Shifrin-Punina (PSP) approximation,
%the function 'Gordon.m' to calculate the Gordon approximation, the
%function 'Mie_approx.m' to calculate the anomalous diffraction
%approximation, 'Mie_angle_intensity.m' to calculate the exact intensity
%at theta unequal to zero, and Matzlers MATLAB-function 'Mie_S12.m' to
%calculate the amplitude functions.

%The program can be modified to use an existing array of
%wavenumbers from experimantal data by uncommenting:
load('Spectra/Wavenumbers.mat');  %load wavenumber array
% load('Spectra/pollen.mat');       %load experimental data
wn = Wavenumbers;                 %wavenumber array

%Choose parameters for the calculations:
eps_r = 1.3^2;       %Real constant part of dielectric constant
dia_m = 22;          %Diametre of sphere(micrometers)
k_min=0;             %Start wavenumber (cm^-1)
k_max=10000;         %End wavenumber (cm^-1)
theta_min = 1;       %Lower integration limit (theta=0 has no contribution)
theta_max = 35;      %Upper integration limit
dia = dia_m*10^-4;   %cm
a = dia/2;           %radius of sphere
%-------------------------------------------------------
%Enter absorption band as a new row: [Lambda, Gamma (imag), k_0 (cm^-1)]
%Calculates the absorption band by:
%eps_imag(k) = Lambda/(k_0^2 - k^2 - Gamma*k)
abs_b = [700000, 20i, 1650;
         550000, 15i, 2500;
```

```
        370000, 50i, 2650];
%-------------------------------------------------
%Generate k-array
k = wn.*2*pi;
% k = k_min:k_max;
k_range = length(k);
%Generates size parameter x-axis:
x_ax=k.*a;
%-------------------------------------------------
Q_fm_g = zeros([1,k_range]);
Q_fm = zeros([1,k_range]);
Q_m = zeros([1,k_range]);
S = zeros([1,k_range]);
%Generates zero angle amplitude function array S(0):
m = sqrt(eps_r);
for i=1:k_range
    x=a*k(i);
    %Collects amplitudes S(0) from Matzlers function Mie_S12.m
    S12=Mie_S12(m, x, cos(0));
    S(i)=S12(1);
end

for theta=theta_min:theta_max
    for i=1:k_range
        eps_imag=eps_r;
        %Include absorption bands in dielectric function by uncommenting:
%         for i=1:length(abs_b(:,1))
%             eps_imag = eps_imag + (abs_b(i,1) /...
%                 (abs_b(i,3)^2 - k^2 - abs_b(i,2)*k));
%         end
        m=sqrt(eps_imag);
        %-----------------------------------------
        %Svitches approximation at given angle theta
        if theta<=10
            I_fm_g = Fymat_Mease(m, k(i), dia_m, theta, S(i));
        else
            I_fm_g = Gordon(m, k(i), dia_m, theta, S(i));
        end
%         I_fm = Fymat_Mease(m, k(i), dia_m, theta, S(i));
%         Q_fm(i) = Q_fm(i) + (2*pi/360)*(2/a^2)*I_fm*sind(theta);
        %-----------------------------------------
        %Calculates approxiamted Q_NA:
        Q_fm_g(i) = Q_fm_g(i) + (2*pi/360)*(2/a^2) * I_fm_g*sind(theta);

        %Calculates exact Q_NA:
        Q_m(i) = Q_m(i) + (2*pi/360)*(2/a^2)...
            * Mie_angle_intensity(m, k(i), dia_m, theta) * sind(theta);

        %Calculates Q_NA by the anomalous diffraction approximation (ADA):
%         Q_m(i) = Q_m(i) + Mie_approx(m, x);
    end
    %To get a reference of progress during time consuming calculations:
    disp(theta);
end
figure(1)
plot(x_ax, Q_fm_g, 'k', x_ax, Q_m, 'b')
xlabel('x=ka');
ylabel('Q_{NA}');
```

B.2 Functions

Listing B.2: Fymat_mease.m

```
function I_fm = Fymat_Mease(m, k, dia, theta, S)
    %Calculates an approximation of mie scattering at a specified angle
    %theta, after the formula proposed by A. L. Fymat and K. D. Mease. The
    %approximation works best for at low angles (theta < 10 deg). By
    %excluding the extension functions proposed by Fymat & Mease, the
    %Penndorf, Shifrin & Punina approximation i calculated. Takes the input
    %arguments: 'm' - the refractive index, 'k' - the wavenumber (cm^-1),
    %'dia' - the diameter of the sphere (micrometers), 'theta' - the angle
    %away form the forward direction (degrees) and 'S' - the forward
    %amplitude function S(0).

    dia = dia*10^-4;
    x = 0.5*dia*k;
    Q_ext = (4/x^2)*real(S);
    g_theta = x*sind(theta);
    %Fraunhofer approximation to the Mie solution
    I_f =  x^4*(besselj(1, g_theta))^2*(1/((k*g_theta)^2));
    %Fymat and Mease constants
    a = 3.63; b = 5.52; c = 6.6; d = 2.4;
    %Generates FM extension functions to the PSP approxmation
    if ((m-1)*x <= a) || ((m-1)*x >= b && (m-1)*x <= c)
        f_1 = (1-besselj(0, (m-1)*x))^-1;
    else
        f_1 = 1;
    end

    if 2*(m-1)*x <= d
        f_2 = (1-besselj(0, 2*(m-1)*x))^-1;
    else
        f_2 = 1;
    end
    %-----------------------------------------------------------
    %Penndorf, Shifrin & Punina formula:
%     I_fm = ((1/2)*Q_ext)^2*I_f;

    %Fymat & Mease formula:
    I_fm = ((1/2)*Q_ext)^2*I_f*f_1*f_2;
```

Listing B.3: Gordon.m

```
function I_g = Gordon(m, k, dia, theta, S)
    %Calculates the intensity at an angle theta from the approximation
    %given by J. E. Gordon. This approximation works best for
    %angles > 10 deg. Takes input arguments: 'S' - the forward
    %scattering amplitude S(0), 'k' - the wavenumber (cm^-1),
    %'dia' - the diameter of the sphere (micrometers), and 'theta' -
    %the angle relative to the direction of the incident light (degrees).

    a = 0.5*dia*10^-4; %cm
    x = a*k;
    x_g = a*k*sqrt(1 + m^2 - 2*m*cosd(theta));
    %Intensity in forward direction
    I_0 = (1/(k^2))*(real(S)^2 + imag(S)^2);
    %-----------------------------------------
    %Modulating function gamma(x):
    gamma = 0.5*(0.3*x_g^(-x/30) + ...
        1.4*x_g^(-x/50)*cosd(theta)^10)*sind(theta/2)^(1/3);

    %Gordons choice of gamma(x):
    % gamma = x_g^(-3/2);
    %-----------------------------------------
    I_g = I_0*((abs(3*(sin(x_g)-x_g*cos(x_g))/x_g^2)/x_g + gamma)^2)...
        * (1+(cosd(theta))^2)/2;
```

Listing B.4: Mie_angle_intensity.m

```
function I_m = Mie_angle_intensity(m, k, dia, theta)
    %Calculates the intensity at an angle theta from the exact Mie
    %scattering amplitudes (S(theta)) by the formula from van de Hulst.
    %Takes the input arguments: 'm' - refractive index, 'k' - wavenumber
    %(cm^-1), 'dia' - diameter (micrometers), 'theta' - angle (degrees).
    %Uses the function Mie_S12.m by C. Matzler.

    a = 0.5*dia*10^-4; %cm
    x = a*k;

    %Real Mie scattering intensity
    S = Mie_S12(m, x, cosd(theta));
    i_1 = abs(S(1))^2;
    i_2 = abs(S(2))^2;
    I_m = (i_1 + i_2)/(2*k^2);
```